

Single-Shot Readout and Weak Measurement of a Tin-Vacancy Qubit in Diamond

Eric I. Rosenthal,^{1,*} Souvik Biswas,^{1,†} Giovanni Scuri,¹ Hope Lee,¹ Abigail J. Stein,¹ Hannah C. Kleidermacher,¹ Jakob Grzesik,¹ Alison E. Rugar,^{1,‡} Shahriar Aghaeimeibodi,^{1,§} Daniel Riedel,^{1,¶} Michael Titze,² Edward S. Bielejec,² Joonhee Choi,¹ Christopher P. Anderson,^{1,3} and Jelena Vučković¹

¹*E. L. Ginzton Laboratory, Stanford University, Stanford, California 94305, USA*

²*Sandia National Laboratories, Albuquerque, New Mexico 87123, USA*

³*Department of Materials Science and Engineering,
University of Illinois Urbana-Champaign, Urbana, IL 61801, USA*

(Dated: March 21, 2024)

The negatively charged tin-vacancy center in diamond (SnV^-) is an emerging platform for building the next generation of long-distance quantum networks. This is due to the SnV^- 's favorable optical and spin properties including bright emission, insensitivity to electronic noise, and long spin coherence times at temperatures above 1 Kelvin. Here, we demonstrate measurement of a single SnV^- electronic spin with a single-shot readout fidelity of 87.4%, which can be further improved to 98.5% by conditioning on multiple readouts. We show this performance is compatible with rapid microwave spin control, demonstrating that the trade-off between optical readout and spin control inherent to group-IV centers in diamond can be overcome for the SnV^- . Finally, we use weak quantum measurement to study measurement induced dephasing; this illuminates the fundamental interplay between measurement and decoherence in quantum mechanics, and makes use of the qubit's spin coherence as a metrological tool. Taken together, these results overcome an important hurdle in the development of the SnV^- based quantum technologies, and in the process, develop techniques and understanding broadly applicable to the study of solid-state quantum emitters.

I. INTRODUCTION

Color center qubits have been recognized as an advantageous platform for the realization of quantum technologies, and in particular quantum networks [1], due to their efficient spin-photon interface, long spin coherence times, and compatibility with nanophotonics [2–4]. An outstanding challenge is to scale quantum networks to include more nodes, greater distance between nodes, and further complexity including error corrected registers of qubits within each node [5].

The path to solving these many challenges is specific to the choice of quantum platform and, in this case, choice of color center. Today, state-of-the-art quantum networks consist of three nodes, where each node is based on a single nitrogen-vacancy center (NV^-) in diamond [6, 7]. However, the NV^- is not the optimal qubit for future quantum networks because of its sensitivity to electrical noise, and a low probability of emission into its zero-phonon line (ZPL), which reduces entanglement generation rate.

Of countless optically active solid-state atomic defects including rare earth ions [8, 9] and defects in silicon carbide [10], group-IV centers in diamond have emerged as promising candidates to advance quantum networks.

These qubits have a centrosymmetric structure, which renders a first-order insensitivity to electrical noise, allowing for relative optical stability even within nanophotonic structures [2]. Advantageously, these color centers also have high quantum efficiency and strong emission into their ZPL, promising high rates of entanglement generation. Among them, the silicon-vacancy center (SiV^-) [11] is the most developed, with demonstrations of long spin coherence times and single-shot electron spin readout [12], integration with nanophotonic cavities [13–17], and demonstration of a two-node quantum network [18].

However, due to its spin-orbit induced ground state splitting of 50 GHz, the SiV^- requires operation at millikelvin temperatures to avoid thermal decoherence [11]. Even then, state-of-the-art demonstrations use highly strained SiV^- 's to increase this splitting and reduce drive induced heating [15–17]. To avoid temperature related issues, the tin-vacancy center (SnV^-) in diamond has emerged as a favorable alternative due to its larger minimum ground state splitting of ≈ 820 GHz [19–24]. This allows for coherent spin control at several Kelvin [25–27], where exponentially more cooling power is available.

Recent advances of the SnV^- platform include incorporation with nanophotonics [28–34], high-fidelity generation of single photons [31, 35], nuclear spin control and single-shot nuclear spin readout [32] enabled by a large hyperfine coupling [36], and high-fidelity microwave spin control using both moderately strained [26] and highly strained [24, 27] centers.

However, recent work on SnV^- spin control has illuminated a complicated relationship between the performance of spin polarization, coherent microwave spin control, and spin readout as functions of strain and the orientation of the applied magnetic field [24, 26, 27, 37, 38].

* These authors share equal contributions; ericros@stanford.edu

† These authors share equal contributions; souvik@stanford.edu

‡ Present address: SandboxAQ, Palo Alto, California 94305, USA

§ Present address: AWS Center for Quantum Computing, San Francisco, California, USA

¶ Present address: AWS Center for Quantum Networking, Boston, Massachusetts, USA

In particular, there is a general trade-off between optimizing for high-fidelity microwave spin control using high strain and certain magnetic field orientations, and optimizing readout using low strain and a magnetic field aligned with the spin dipole axis. To-date, the only published demonstration of single-shot readout of an SnV^- 's electronic spin uses an unstrained center not favorable for coherent spin control [39], and the only demonstrations of coherent spin control use readout far from the single-shot regime [24–27]. This brings into question if rapid spin control *and* high-fidelity readout are compatible for the SnV^- , as has previously been shown for the SiV^- [12].

In this article, by precise study of readout performance and associated trade-offs (Fig. 1), we answer this question favorably and further our understanding about both the SnV^- platform and, in general, about the quantum measurement of solid-state emitters. We demonstrate measurement of a single SnV^- electronic spin with a single-shot readout fidelity of 87.4% at the same operating conditions as rapid microwave spin control. We also report a conditional readout fidelity of 98.5% by conditioning on the outcome of two consecutive measurements. We achieve this performance using an overall measurement efficiency of $\approx 0.1\%$, implying that near-unit fidelity is achievable in future nanophotonic devices that have much greater efficiency. Finally, we use a combination of coherent spin control and weak quantum measurement to study measurement induced dephasing — both affirming the basic science of quantum measurement, and, using the qubit's spin superposition as a resource to benchmark its interaction with light and characterize the measurement apparatus. The understanding and methods developed in this work will advance SnV^- based quantum technologies, will enable the use of an SnV^- 's long spin coherence time as a resource for quantum memory, and will have broad application to the study and measurement of a wide class of solid-state quantum systems.

II. SPIN STATE PREPARATION AND CONTROL

A. Optical transitions

Of crucial importance to the measurement of any qubit is its Hamiltonian. For group-IV color centers in diamond, the Hamiltonian [40] is set by both strain of the diamond lattice and by \vec{B} , the external magnetic field. Here we study the same SnV^- used in Ref. [26], which has a ground state splitting of 903 GHz, larger than that of an unstrained SnV^- . This is in a regime of “moderate” strain, where the ground-state strain (≈ 355 GHz) is non-negligible but less than the spin orbit coupling.

To understand the importance of magnetic field orientation, we first consider the SnV^- 's two lowest energy levels $|\downarrow\rangle$ and $|\uparrow\rangle$ in the ground state manifold, and the two lowest energy levels $|A\rangle$ and $|B\rangle$ in the excited state

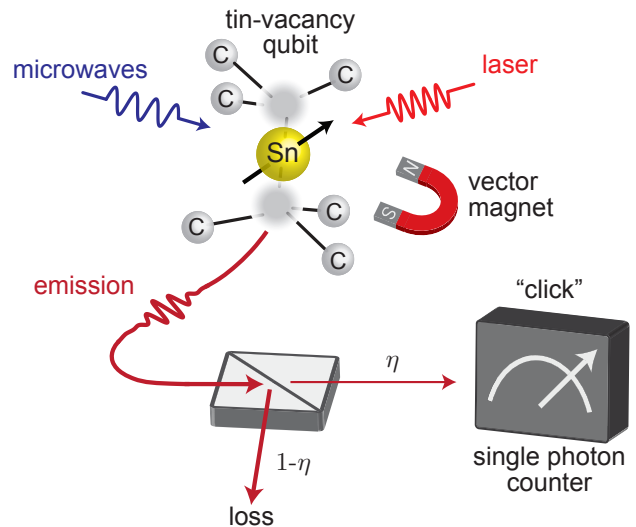


FIG. 1. **Schematic.** A tin-vacancy (SnV^-) qubit consists of a tin atom replacing two carbon atoms in a diamond lattice. Here, we manipulate the spin of this atom-like system under application of a static magnetic field, and using a combination of optical and microwave control pulses. This leads to spin-dependent photoluminescence, which we measure using a single photon counter. The presence or absence of “clicks” on the detector is used to determine the qubit’s spin state with high fidelity. Even so, some emission is lost via different channels before detection; this loss is parameterized by a beamsplitter with transmittivity η placed between the qubit and an idealized detector. Here η is the overall measurement efficiency.

manifold, Fig. 2a. Both sets of levels split with magnetic field due to the Zeeman effect, which can lead to four distinct transitions as shown in Fig. 2a: A1 and B2 (“spin-preserving”), and A2 and B1 (“spin-flipping”) [11]. The detuning between these transitions is highly dependent on the alignment between the magnetic field \vec{B} and the magnetic spin dipole $\vec{\mu}$, parameterized by the angle ζ , which is the angle of the vector \vec{B} in the plane defined by our two-axis magnet with coils along the \hat{x} and \hat{z} directions (see Fig. 2b). The dipole axis is defined by the crystallographic symmetry axis that connects two missing carbon atoms and an interstitial tin vacancy (see Fig. 1). The angle φ is a measure of misalignment between the dipole and magnetic field plane, and we have tried to minimize this angle by physical rotation of the sample.

The A1 and B2 transitions are characterized using photoluminescence excitation (PLE) spectroscopy, Fig. 2c, by sweeping ζ for a magnetic field of fixed amplitude $|\vec{B}| = 180$ mT. Data in Fig. 2 are modelled by the Hamiltonian described in Table. I of Ref. [24]. See Appendix B1 for details, including discussion of free parameters and modifications to the SnV^- Hamiltonian reported by our previous work, Ref. [26].

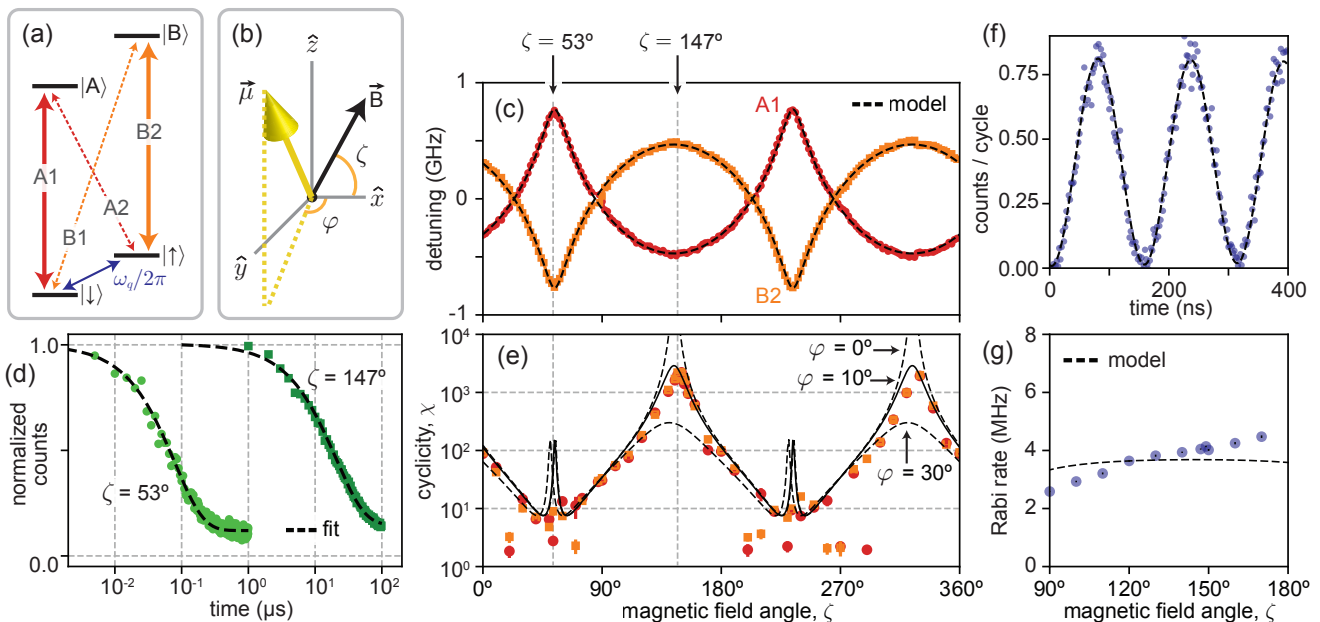


FIG. 2. **Spin-selective state initialization and optical and microwave control.** (a) Simplified energy level diagram of the tin-vacancy qubit (SnV^-) in diamond. Electron spin ground states $|\downarrow\rangle$ and $|\uparrow\rangle$ are separated by the qubit frequency $\omega_q/2\pi$. Red and orange lines illustrate optical transitions to the excited states $|A\rangle$ and $|B\rangle$. These transitions are either spin-preserving (A1 and B2), or spin-flipping (A2 and B1). (b) The spin, with magnetic dipole $\vec{\mu}$, interacts with a magnetic field \vec{B} via the Zeeman effect. Here, \vec{B} is oriented at the angle ζ in the plane defined by the \hat{x} and \hat{z} coordinates. The spin is oriented at azimuthal angle φ from this plane. (c) Photoluminescence excitation (PLE) measurement of the A1 and B2 transitions vs ζ , fixing $|\vec{B}| = 180$ mT. Detuning is measured from 619.13972 nm (484.20808 THz). (d) Driving a spin-preserving transition polarizes the spin at rate κ (data shown for driving A1). This rate is also dependent on ζ . (e) Cyclicity (the ratio of the probabilities of spin-preserving to spin-flipping decay) vs. ζ , determined from a fit of κ applied to Eq. 1 in the high power limit. Here, cyclicity changes by three orders-of-magnitude depending on ζ , up to $\chi \approx 2.5 \times 10^3$. Cyclicity is expected to diverge when \vec{B} and $\vec{\mu}$ align; here it is limited by the minimum misalignment φ , set to $\varphi = 10^\circ$ for a model which follows our data (solid black line). (c) and (e) share an x-axis. (f) Rabi oscillations between the ground spin states under microwave driving, demonstrating an 80 ns π -pulse time at $\omega_q/2\pi = 3.677$ GHz. (g) Microwave Rabi rate vs. ζ . At each angle, the amplitude $|\vec{B}|$ is tuned so that $\omega_q/2\pi = 4.00$ GHz. Data are compared to a model [26] that uses a microwave field of amplitude 0.6 mT oriented perpendicular to $\vec{\mu}$.

B. Cyclicity

In addition to setting the detuning between the A1 and B2 transitions, the magnetic field orientation controls the *cyclicity*; a crucial parameter for understanding spin measurement. When pumped to $|A\rangle$ or $|B\rangle$, the SnV^- subsequently relaxes to its ground state in a manner which can preserve the spin, i.e. by decay via the A1 or B2 transitions with probabilities P_{A1} or P_{B2} , respectively. Alternatively, its spin can flip: i.e. by decay via the A2 or B1 transitions with probabilities P_{A2} and P_{B1} , respectively. Cyclicity $\chi = P_{A1}/P_{A2} = P_{B2}/P_{B1}$ is the ratio of the probability of spin-preserving decay to spin-flipping decay.

Cyclicity determines how many photons are emitted, corresponding to the maximum allowed number that can be collected during readout, and the optimal readout duration. For a given excitation power, a higher χ indicates more photons can be collected before the spin polarizes and goes “dark” (no longer emits photons). However, in

trade-off, a longer duration of optical drive is required to polarize the spin state. A smaller χ will lead to faster polarization, but will limit the number of emitted photons and the useful duration of acquisition.

For example, if the SnV^- is prepared in the $|\downarrow\rangle$ state given by density matrix $\hat{\rho} = |\downarrow\rangle\langle\downarrow|$ and driven on A1 starting at time $t = 0$, it will polarize into $|\uparrow\rangle$ at rate κ such that $\hat{\rho}(t) = e^{-\kappa t} |\downarrow\rangle\langle\downarrow| + (1 - e^{-\kappa t}) |\uparrow\rangle\langle\uparrow|$. Here,

$$\kappa = \frac{R}{\chi + 1}, \quad (1)$$

is the polarization rate and,

$$R = \frac{\gamma}{2} \left(\frac{p/p_{\text{sat}}}{1 + p/p_{\text{sat}} + (\frac{\delta}{\gamma/2})^2} \right), \quad (2)$$

captures an effective optical pumping rate to $|A\rangle$, which depends on drive power p , on-resonance saturation power p_{sat} , and detuning δ of the drive from the transition.

Eq. 1 follows from the optical Bloch equations [41], see Appendix A 1 for details. For the SnV^- , $\gamma \approx (4.5 \pm 0.2 \text{ ns})^{-1} = 2\pi \times (35 \pm 1.6 \text{ MHz})$ is the optical decay rate [22].

Intuitively, at $p/p_{\text{sat}} \gg 1$ and $\delta \lesssim \gamma$, the rate of excitation to the higher state is much faster than relaxation, thus $\kappa \approx \gamma/2\chi$ is independent of power but is proportional to the saturated optical decay rate and inversely proportional to cyclicity. At $p/p_{\text{sat}} \ll 1$, however, the excitation rate is much slower than relaxation, and $\kappa \approx (\gamma/2\chi) \times (p/p_{\text{sat}})$ is also proportional to power.

We experimentally measure κ by binning the time-tagged photon counts collected during resonant excitation. The number of collected counts decays exponentially: $(\Gamma_{\text{max}} - \Gamma_{\text{min}})e^{-\kappa t} + \Gamma_{\text{min}}$, and data in Fig. 2d is fit to this exponential model to determine κ . Here $t = 0$ is the onset of excitation, Γ_{max} is the maximum count rate, and Γ_{min} is the mean count rate at $t \gg 0$. The term $(\Gamma_{\text{max}} - \Gamma_{\text{min}})e^{-\kappa t}$ captures signal from SnV^- emission, and the background Γ_{min} arises from noise dominated by unwanted scatter of excitation light into collection and detector dark counts. Cyclicity $\chi \approx \gamma/2\kappa$ is determined from κ via Eq. 1. For data in Fig. 2 we operate at negligible detuning (the drive frequency is re-calibrated at each point) and at powers far above saturation.

Both κ and χ are highly dependent on the alignment between \vec{B} and $\vec{\mu}$. This is characterized in Fig. 2e by measuring χ vs. the angular orientation of \vec{B} along angle ζ . Cyclicity changes by three orders of magnitude during this sweep. At $\zeta = 147^\circ$ near where alignment is maximum, we measure $\kappa = (20.4 \pm 0.30 \mu\text{s})^{-1} = 49.02 \pm 0.72 \text{ kHz}$ corresponding to $\chi = 2244 \pm 108$. At similar power and at $\zeta = 53^\circ$ where alignment is near minimum, we measure $\kappa = (78.5 \pm 0.002 \text{ ns})^{-1} = 12.74 \pm 0.0004 \text{ MHz}$ and determine $\chi = 8.6 \pm 0.4$. The difference between ζ values corresponding to maximum and minimum cyclicity differs from exactly 90° ; we postulate this is due to slight miscalibration of one or both magnetic coils, such that amplitude $|\vec{B}|$ is also changing slightly with ζ .

When \vec{B} and $\vec{\mu}$ are perfectly aligned, spin-flipping relaxation becomes entirely forbidden, and cyclicity is expected to diverge ($\varphi = 0$ model in Fig. 2e). The extent to which it does not indicates remaining misalignment, e.g. the spin dipole $\vec{\mu}$ is rotated by azimuthal angle φ relative to the plane defined by the axes \hat{x} and \hat{z} , Fig. 2b. Our data follow a model using a misalignment of $\varphi = 10^\circ$ (solid black line, Fig. 2e). This suggests cyclicity can be increased by fine tuning sample rotation and/or by using a three-axis vector magnet.

Cyclicity is minimal when $\vec{B} \cdot \vec{\mu} \approx 0$. However, the models in Fig. 2e (based on the model in Ref. [26]) show a slight increase in cyclicity around maximal misalignment. This feature is due to the re-definition of the spin's quantization axis along the direction of strain. Finally, we notice that for some of the angles the data differs from the model where points of lowest cyclicity occur near the angles where the A1 and B2 transitions become degenerate. We postulate this effect could be due to a cou-

pling interaction between these transitions indicative of a previously unexplored term in the SnV^- Hamiltonian; further investigation is necessary to understand this phenomenon.

C. Spin polarization fidelity

Measurement of spin polarization, as in Fig. 2d, also bounds the polarization fidelity. This quantifies the extent to which a resonant drive prepares the qubit in the pure states $|\downarrow\rangle$ or $|\uparrow\rangle$, and is defined as $F_{\text{pol}} = 1 - \frac{1}{2}\Gamma_{\text{min}}/\Gamma_{\text{max}}$, where Γ_{max} is the maximum count rate and Γ_{min} is the mean count rate in the $t \gg 0$ limit [22, 25]. We measure $F_{\text{pol}} = 92.8\%$ at $\zeta = 147^\circ$, and $F_{\text{pol}} = 94.9\%$ at $\zeta = 53^\circ$, consistent with other examples of high-fidelity spin polarization of SnV^- 's [22, 25–27, 39]. This is limited by non-zero Γ_{min} , which is dominated by scattering from the excitation laser into the collection path. This technical source of noise can be mitigated by better spectral filtering, and thus our polarization fidelity measurement is a lower bound.

D. Spin control

We now characterize performance of the SnV^- as a spin qubit. When operated at maximum cyclicity ($\zeta = 147^\circ$) we demonstrate high-fidelity spin manipulation using a microwave control pulse, Fig. 2f. At this operating point we demonstrate a π -pulse time of 80 ns, operated at $\omega_q/2\pi = 3.677 \text{ GHz}$ (with $|\vec{B}| = 125 \text{ mT}$) and using microwave input power and packaging similar to Ref. [26].

In Fig. 2g we also measure the Rabi rate (defined as the inverse of twice the π -pulse time), as a function of ζ . To avoid frequency dependent changes to microwave power delivery, we keep the qubit frequency fixed at $\omega_q/2\pi = 4.000 \pm 0.002 \text{ GHz}$ by changing the amplitude $|\vec{B}|$ at each value of ζ . Data is compared to a model (from Ref. [26]) that assumes a drive of $|\vec{B}| = 0.6 \text{ mT}$ at the spin location, and which is oriented perpendicular to $\vec{\mu}$. For this drive orientation, the Rabi rate is expected to be highest near $\approx 147^\circ$ where \vec{B} and $\vec{\mu}$ are maximally aligned, and symmetric with angle around this operating point. Disagreement between theory and experiment may be due to drifting microwave power delivery, and/or, miscalibration of one or both magnetic coils. However, the main result of Fig. 2g is that microwave Rabi rate changes little with ζ . Therefore, at least for this level of strain, SnV^- experiments can expect to operate at optimal cyclicity without compromise to microwave spin control.

In summary, we have determined that resonant excitation polarizes the SnV^- spin state while inducing photon emission. These effects have a strong dependence on the alignment between the spin dipole and external magnetic field, with closer alignment leading to slower

polarization, higher cyclicity, and greater emission. We also demonstrate that high cyclicity is compatible with rapid microwave spin control. For the remainder of this work we operate at $\zeta = 147^\circ$ where cyclicity is maximized for this experimental setup.

III. READOUT CHARACTERIZATION

A. Readout fidelity

Given our understanding of spin polarization and cyclicity, we now characterize readout of the SnV^- spin state. To do so, we measure the time-tagged photon statistics of two subsequent readout steps, Fig. 3a. Depending on spin state preparation, the histogram of counts collected over many readout events in a set window follows either a “bright” distribution with a mean photon number of $\bar{n}_b > 0$, or a “dark” distribution with a mean photon number $\bar{n}_d \approx 0$.

Readout fidelity is defined as [42]:

$$F_r = 1 - \frac{1}{2}P(1|\downarrow) - \frac{1}{2}P(0|\uparrow), \quad (3)$$

Here, $P(0|\uparrow)$ is the error probability of the measurement outcome “0” (down state), when the qubit had been initialized in $|\uparrow\rangle$. Similarly, $P(1|\downarrow)$ is the error probability of the measurement outcome “1” (up state), when the qubit had been initialized in $|\downarrow\rangle$. These errors are determined by the number of counts during a given readout event falling to either side of a discrimination threshold N_r , chosen to maximize F_r .

Readout results are shown in Fig. 3b,c. After spin state initialization, two subsequent readout steps separated by a microwave π -pulse (“wfm-A”), or with no pulse (“wfm-B”). In each readout step the resonant laser is pulsed for $100 \mu\text{s}$, long enough to fully polarize the spin state. However emitted counts are only recorded for the first $50 \mu\text{s}$ of this drive, since after this time the noise (predominantly scatter from the excitation laser) can exceed the emitted signal and thus reduce fidelity. For both the first and second readout steps we measure a readout fidelity of $F_r = 87.4\%$. This is in the “single-shot” regime, meaning a single projective measurement, or experimental “shot”, correctly determines the qubit with this fidelity. For this measurement, the “dark” distribution has $\bar{n}_d \leq 0.2$ counts per cycle, and “bright” distributions have $\bar{n}_b \approx 4$ counts per cycle.

Both before and after these readout steps, we include charge resonance checks [42] (CRCs, not shown in Fig. 3a). Each CRC is a spin-independent check that consists of simultaneously driving both spin-preserving transitions (A1 and B2), and recording the check as a pass only if greater than a certain number of counts are collected during the check (see Appendix C3b for details). Importantly, CRCs allow us to selectively characterize our qubit only when it is in the correct charge

state and not suffering from spectral diffusion. For example cycles are not recorded when the qubit “blinks off” – an erasure error that can be caused by the excitation laser changing the defect’s charge state. By setting a CRC pass threshold to maximize readout fidelity while keeping a significant fraction of cycles, we retain 7.4% (7.7%) of cycles of wfm-A (wfm-B), out of 4.27×10^5 cycles total for each waveform. The data shown in Fig. 3 includes passing cycles, only. See Fig. 13 for analysis of readout as a function of pass threshold.

B. Conditional fidelity

Readout can be further characterized by a “conditional fidelity”, F_c , which conditions on the results of two subsequent measurements. For example, consider the characterization sequence described in Fig. 3a. The result of these two measurements should be anti-correlated due to the insertion of the spin π -pulse during the second readout, enabling the extraction of the conditional fidelity. We therefore expect results “1” then “0” for wfm-A, and results “0” then “1” for wfm-B. Using the data in Fig. 3d we find a conditional fidelity of $F_c = 98.5\%$, defined as [43, 44]:

$$F_c = \frac{P(j|i)}{P(i|j) + P(j|i)}. \quad (4)$$

Here, $i, j \in \{0, 1\}$ are measurement results with $i \neq j$, and $P(j|i) \geq P(i|j)$ are the conditional probabilities of result i (j) in the second readout given result j (i) in the first readout. Like CRCs, conditional fidelity provides an avenue to retain data to only include select experimental cycles. This boosts the fidelity of selected measurements at the cost of a reduced rate of data acquisition.

C. Quantum non-demolition fidelity

Correlating the results of two subsequent measurements also quantifies the degree to which readout is quantum non-demolition (QND) [45, 46]. In quantum theory, a qubit which has been projectively measured should remain in its measured eigenstate [47]. This is a desirable property; for example, it is needed in quantum error correction algorithms that require an ancilla qubit to be repeatedly measured.

However, a realistic quantum measurement is not always QND. For example, a measurement that correctly determines a color center’s spin state, but in the process kicks the color center into a different charge state and thus out of the qubit subspace (erasure error), is *not* QND. A measurement which heats the qubit, causing bit flip errors independent of the measurement result is also *not* QND.

The SnV^- qubit and many other atom-like systems have the property that, due to spin polarization under resonant drive, when the qubit is measured in the

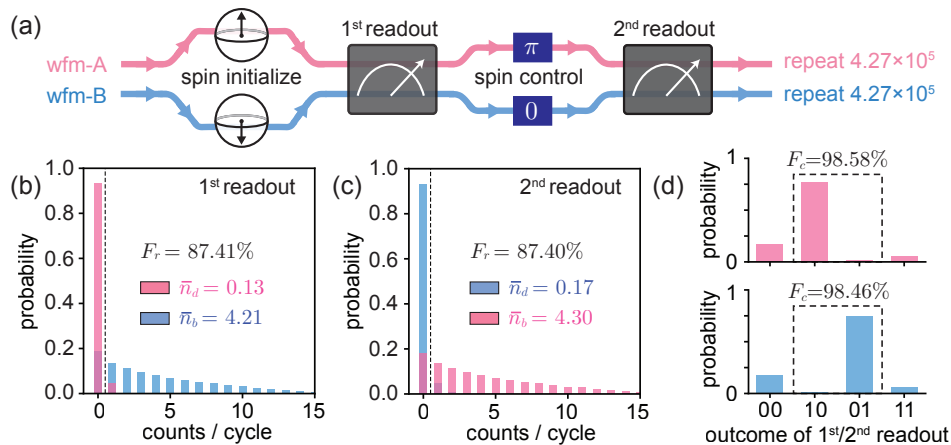


FIG. 3. **Single-shot readout of a single electron spin.** (a) Readout is characterized using two waveforms (wfm-A and wfm-B) which are each repeated for 4.27×10^5 cycles. Each cycle begins with preparation of the spin in the polarized states $|\uparrow\rangle$ or $|\downarrow\rangle$ (wfm-A or wfm-B, respectively). The spin state is then projectively measured twice. Between measurements the spin is either coherently flipped by a microwave π -pulse (wfm-A), or, no pulse is applied (wfm-B, where readout of spin-down state already flips the spin). Each cycle also includes two charge resonance checks (CRCs; not shown, see Fig. 11 for details). (b,c) Count distributions of the first and second readouts, respectively. Lower (higher) number distributions have a mean count number of \bar{n}_d (\bar{n}_b) and are associated with the projection of the qubit in the $|\uparrow\rangle$ ($|\downarrow\rangle$) states prior to measurement. A given readout event yields the result “1” (“0”) if the counts collected during this event fall below (at or above) a threshold $N_r = 1$, illustrated here by the black dashed lines. Here, both readout steps have a fidelity of $F_r = 87.4\%$ (Eq. 3) and (d) a conditional fidelity of $F_c \approx 98.5\%$ (Eq. 4). Note that data in (b,c,d) has been post-selected for cycles which pass both CRCs (7.7% of cycles for wfm-A, and 7.4% of cycles for wfm-B, see Fig. 12 for details).

spin state associated with bright emission its eigenstate is also flipped. Therefore the SnV⁻ readout described in this work is not QND by the definition $F_{\text{QND}} = [P(1|1) + P(0|0)]/2$ [45], where $P(1|1)$ and $P(0|0)$ are the conditional probabilities that subsequent measurements each yield the same result. However, we may define an alternate definition that captures the extent to which a qubit remains in the eigenstate it *should* be in after measurement (i.e. is not subject to erasure error, or an unexpected bit-flip error). We define this QND-equivalent fidelity, F_q , as:

$$F_q = \frac{1}{2} [P(i|j) + P(j|i)], \quad (5)$$

where $i, j \in \{0, 1\}$ and $i \neq j$. Here, $P(i|j)$ and $P(j|i)$ are the conditional probabilities that subsequent readout results are anti-correlated as they are expected to be for the experimental sequence in Fig. 3a. Eq. 5 therefore captures the essence of QND fidelity; the extent to which readout does not unexpectedly perturb the qubit. After all, a measurement result which deterministically flips the qubit state can in-principle be corrected by a π -pulse to return the qubit to its measured state, and would thus be QND by the standard definition [45].

Using Eq. 5, we compute $F_q = 76.3\%$ for the data in wfm-A and $F_q = 77.9\%$ for the data in wfm-B. Post-measurement, the qubit therefore remains in its expected eigenstate a considerable fraction of the time. Infidelity is dominated by cycles in which both readouts yield a dark result, which may result from blinking of the qubit dur-

ing readout even for cycles when both CRCs are passed, or, from the non-zero overlap of the bright and dark distributions. Finding ways to increase F_q is an important research direction for future experiments and is key to implement many quantum error correction protocols.

D. Efficiency

The electron spin readout described in Fig. 3 is not perfect, as evidenced by the overlap of the distributions in Fig. 3b,c. In this section we study what limits the number of collected photons, including characterizing the “measurement efficiency”, η , that quantifies overall loss between the qubit and detector.

Here we define measurement efficiency to be equivalent to a beamsplitter with transmission η placed between a source of emission and an ideal photon counter, Fig. 1. This is the probability of detecting a “click” per emission event, and is the product of the probability of all sources of loss. It is crucial to characterize and understand η in order to improve future experiments by reducing loss. Lower loss (increased η) will allow for higher fidelity single-shot readout and in future quantum networks will allow improved rates of entanglement generation.

Cyclicity describes the number of times, on average, that the emitter goes through excitation / relaxation before polarizing. From Fig. 2d,e we expect $\chi \approx 2.2 \times 10^3$ emission events per readout, assuming the duration of

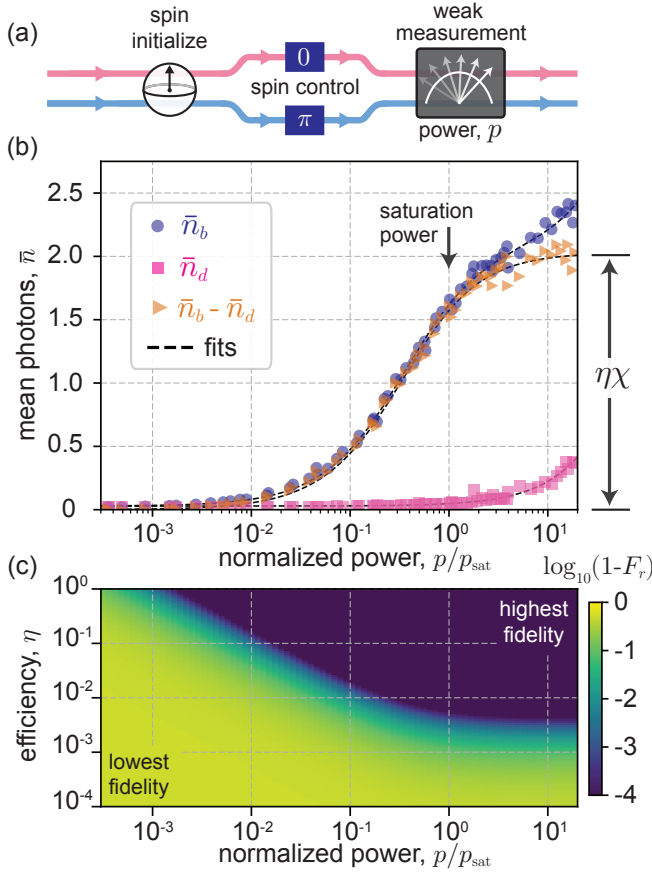


FIG. 4. **Measurement dependence on power and efficiency.** (a) Readout performance is characterized as a function of measurement power p . Data is post-selected on a charge resonance check (CRC) before each cycle, not shown. (b) Mean counts \bar{n}_b and \bar{n}_d in the bright or dark distributions, respectively, plotted vs. normalized power p/p_{sat} , where p is the optical drive power and p_{sat} is the on-resonance saturation power. The difference $\bar{n}_b - \bar{n}_d$ captures signal from emitted photons, and is fit to Eq. 6 to obtain a saturation power of $p_{\text{sat}} = 313 \pm 8$ nW and a measurement efficiency of $\eta = 0.1\%$. (c) Simulated readout infidelity $1 - F_r$, plotted on a log scale. Here F_r is simulated using Eq. A20 which assumes emission to follow Poissonian statistics, and assumes $\chi = 2.2 \times 10^3$ as in experiment. Greater efficiency lowers the drive power needed to achieve high fidelity.

readout is long compared to the polarization time. We measure far fewer counts per readout because most emission events are not recorded by our detector. From the qualitative argument that $\eta \approx \bar{n}_b/\chi$ and $\bar{n}_b \approx 4$, we estimate $\eta \approx 0.2\%$ for the data in Fig. 3.

To further this argument, we compare the power dependence of emission to the model (Appendix A 1):

$$\bar{n}_b - \bar{n}_d = \eta\chi(1 - e^{-\kappa\tau}), \quad (6)$$

which assumes preparation in the spin state associated with bright emission, and at high power simplifies to $\bar{n}_b - \bar{n}_d \approx \chi\eta$. Here, κ is the power-dependent polarization

rate, $\chi = 2244 \pm 108$ is the cyclicity, $\tau = 50 \mu\text{s}$ is the duration of the readout collection window, and as before \bar{n}_b (\bar{n}_d) are the mean number of counts detected when the qubit is prepared in the spin state associated with bright (dark) emission.

We fit Eq. 6 to the measurement in Fig. 4b. From this fit we determine efficiency of $\eta = 0.992 \times 10^{-3} \pm 5.73 \times 10^{-6} \approx 0.1\%$; this is lower than we expect from the data in Fig. 3 because of the lower mean count number difference of $\bar{n}_b - \bar{n}_d \approx 2$ collected photons per cycle at high powers. We attribute this difference to changing conditions of the setup between measurements including drift in alignment and fluctuating polarization of the excitation laser.

Fig. 4b shows that the mean number of emitted photons plateaus near a saturation power of $p_{\text{sat}} = 313 \pm 8$ nW, specified at the input to the cryostat. This affirms the straightforward conclusion that readout should be optimized by operating near saturation. Below saturation, emission can be increased by pumping harder. Above saturation, noise may increase with power but signal will not. See Fig. 10 for a measurement of readout fidelity vs. power.

Many sources of loss contribute to inefficiency including non-radiative decay, filtering of emission to collect the phonon sideband only, loss between the qubit and detector, and detector inefficiency (see Table II for details). However, we estimate the dominant source of loss is the scattering of emission into bulk diamond rather than into the collection path. Although this is the same emitter used in Ref. [26], from fine-tuned optimization using nano-positioners we confirm that this emitter is actually in a mesa structure (see Fig. 9) rather than a photonic nanopillar. Numerical simulations of an SnV^- center within this structure predict that only a modest $\approx 5\%$ of emitted light is routed to collection (compared to $\approx 3\%$ for an emitter in bulk).

This fraction can be greatly increased by use of nanophotonics. For example, at visible wavelengths, an emitter integrated with a waveguide can allow for $\approx 45\%$ of channelling of photons into the waveguide mode [48]. For 1D photonic crystal nanobeams, this number can be increased to $\approx 90\%$ [29]. Likewise, inverse-designed grating couplers can extract $\approx 25\%$ [49] and tapered fiber coupling up to $\approx 90\%$ [50] of photons in a waveguide mode. Since stable, narrow linewidth SnV^- 's have already been successfully incorporated into nanophotonic structures [28–34], utilizing nanophotonics offers a clear path toward an order-of-magnitude higher efficiency. This will allow for much higher spin readout fidelity, Fig. 4c, over expanded magnetic field orientations and strain regimes. For instance, this will enable single-shot readout of highly strained SnV^- 's (with lower cyclicity), for which microwave spin control requires less drive power [24, 27].

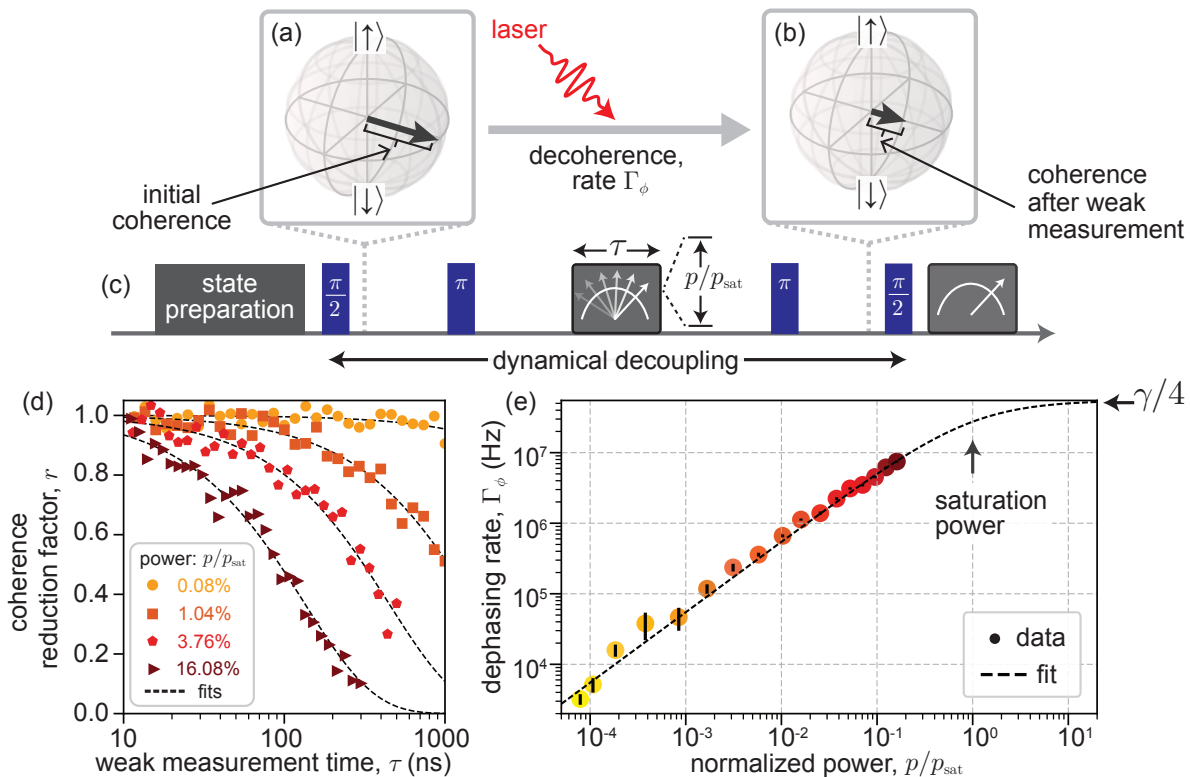


FIG. 5. **Control of qubit dephasing via weak quantum measurement.** (a) A qubit prepared in a superposition state has an initial *coherence*, specified by the amplitude of its off-diagonal density matrix elements $|\hat{\rho}_{\downarrow\uparrow}|$. This is illustrated on the Bloch sphere for the superposition state $(|\downarrow\rangle + |\uparrow\rangle)/\sqrt{2}$. (b) Measurement causes decoherence at rate Γ_ϕ . In a projective measurement the qubit is entirely dephased, but more generally after a weak measurement its coherence is reduced to $|\hat{\rho}'_{\downarrow\uparrow}| \leq |\hat{\rho}_{\downarrow\uparrow}|$. (c) This interplay is studied by inserting a weak measurement of variable power p/p_{sat} and variable duration τ into the center of a dynamical decoupling experiment. (See Fig. 11 for details.) The (projective) readout signal of this experiment measures the ratio r of the remaining coherence to the initial coherence, $r = |\hat{\rho}'_{\downarrow\uparrow}|/|\hat{\rho}_{\downarrow\uparrow}|$, which decays exponentially with weak measurement time as $r = \exp(-\Gamma_\phi\tau)$. (d) Selected measurements of r as a function of τ and p/p_{sat} , and compared to exponential fits. (e) Dephasing rate vs. power. Below saturation, the dephasing rate rises linearly with power. Above saturation, it plateaus to $\gamma/4$, the maximum dephasing rate set by the SnV⁻'s optical decay rate γ . Data are fit to Eq. 7.

IV. WEAK MEASUREMENT OF A COLOR CENTER QUBIT

A. Controlled dephasing

Aside from the practical use of characterizing efficiency and optimizing readout, Fig. 4 illustrates that the power dependence of readout offers a broad pathway for exploring quantum measurement. Measurement is fundamental to quantum theory, and is taken as one of the axioms of quantum mechanics [47]. Under the action of measurement, a quantum state undergoes probabilistic collapse into one of its eigenstates. This collapse destroys quantum superposition, i.e. causes decoherence.

After a *projective* measurement, for example as demonstrated in Fig. 3, a measured quantum state is entirely dephased and is projected into a classical, probabilistic mixture of eigenstates. In contrast, for the case of a *weak* measurement [51], a quantum state has a finite chance of collapse and therefore, on average, retains some coher-

ence. This equivalently limits the classical information a detector may acquire about its state. In this section, we combine the techniques we have thus far demonstrated: high-fidelity spin control (Fig. 2), single-shot projective measurement (Fig. 3) and weak measurement (Fig. 4) in order to study measurement induced dephasing of the SnV⁻'s electronic spin, Fig. 5. This study is an interesting parallel to recent work in the superconducting qubit community, e.g. [51–55], and contrasts from previous color-center based work focused on nuclear spin control [56–59].

To study measurement induced dephasing we do the experiment described in Fig. 5: the qubit is prepared in a superposition state with initial coherence $|\hat{\rho}_{\downarrow\uparrow}|$, subjected to a weak measurement, and finally, projectively measured to determine its remaining post-measurement coherence, $|\hat{\rho}'_{\downarrow\uparrow}|$. The weak measurement pulse consists of a resonant laser drive of power p and duration τ , and is placed at the center of a dynamical decoupling sequence (see Fig. 11d for details). As τ and p increase we ob-

serve a decrease in readout contrast, which is proportional to the qubit's remaining coherence after undergoing weak measurement. We fit this to the exponential model $|\hat{\rho}'_{\downarrow\uparrow}| = |\hat{\rho}_{\downarrow\uparrow}|e^{-\Gamma_\phi\tau}$, where Γ_ϕ is the measurement induced dephasing rate.

We fit the measurement of Γ_ϕ as a function of power, Fig. 5d, to the model (see Appendix A 1):

$$\Gamma_\phi = \frac{R}{2}, \quad (7)$$

where R is given by Eq. 2. Notice there is a simple relationship $\Gamma_\phi \approx \chi\kappa/2$ between Eq. 1 and Eq. 7. Polarization, dephasing, and emission are all closely related with power dependence governed by the relative ratio of pump power to its saturation value, $p/(p + p_{\text{sat}})$, as follows from the optical Bloch equations, and with the overall timescale of dynamics set by the optical decay rate γ .

This experiment offers a way to precisely study how strongly the laser drive interacts with a qubit. In the low power limit, dephasing rises linearly with p . Above saturation, dephasing must plateau to the limit controlled by the optical decay rate, γ . A fit of Eq. 7 to the data in Fig. 5d determines a saturation power of $p_{\text{sat}} = 1436 \pm 21$ nW, specified at the input to the cryostat. We attribute the difference between p_{sat} here compared to the measurement in Fig. 4 to drift in the optical setup between datasets, and/or, that the data in Fig. 4 is post-selected on CRCs whereas data in Fig. 5 is not.

B. A general method to characterize efficiency

Apart from the fundamental scientific curiosity surrounding study of quantum measurement, examining the low power limits of measurements depicted in both Fig. 3c and Fig. 5d offers an alternative means to evaluate measurement efficiency. Far below saturation, both the mean photon count difference $\bar{n}_b - \bar{n}_d$ and the measurement induced dephasing rate Γ_ϕ scale linearly with power. Taylor expanding Eq. 6 in the $p/p_{\text{sat}} \ll 1$ limit and for $\delta = 0$ gives: $\bar{n}_b - \bar{n}_d = Ap + \mathcal{O}(p^2)$ with proportionality constant $A = \gamma\eta\tau/(2p_{\text{sat}}) = 1.744 \times 10^{-2} \pm 8.305 \times 10^{-5}$ nW⁻¹. At low power, $\Gamma_\phi = Bp + \mathcal{O}(p^2)$ is also linear with proportionality constant $B = \gamma/(4p_{\text{sat}}) = 41.5 \pm 2.4$ kHz/nW. Therefore,

$$\eta = \frac{A}{2B\tau}, \quad (8)$$

where A is a fit of Eq. 6 to the weak measurement data in Fig. 4b, and B is a fit of Eq. 7 to the measurement induced dephasing data in Fig. 5e, and $\tau = 50$ μ s is the readout integration window. See Ref. [52] for a similar approach for characterizing the efficiency of superconducting qubit measurement.

Here, solving Eq. 8 gives $\eta = 0.420\% \pm 0.024\%$. This is greater than the fit to the data in Fig. 4c alone, and is

consistent with the greater saturation power of the data in Fig. 5d. This indicates the laser is interacting less strongly with the qubit in the dataset used to fit B , which we postulate is due to differences in the measurement conditions between these experiments.

Despite this difference, we include Eq. 8 because it provides a general framework that may be useful in future experiments requiring precise characterization of solid-state atomic systems. This measurement allows for determination of efficiency within the low power limit, thus avoiding the effect of power-dependent qubit instability. It may be particularly applicable to other color centers which are difficult to saturate or have a competing ionization process.

V. CONCLUSION

In conclusion, we demonstrate single-shot readout of a single electronic spin of an SnV⁻ qubit in diamond, along with coherent control of this spin by a microwave drive. We report a readout fidelity of $F_r = 87.4\%$ using a 50 μ s readout integration window. These results are achieved by aligning the magnetic field near the spin dipole direction (misalignment of $\varphi \approx 10^\circ$) to operate at cyclicity $\chi \approx 2200$. To our knowledge this is highest fidelity single-shot readout of an SnV⁻ spin that has been published to-date: the readout in Ref. [39] reports a lower fidelity of 74%, and uses an un-strained emitter for which microwave spin control is not feasible. (Ref. [32] reports readout of an SnV⁻ nuclear spin, and also does not include spin control.) Next, using high-fidelity readout we repeatedly measure the qubit and characterize the extent to which subsequent measurements are correlated; doing so we characterize a conditional fidelity of $F_c = 98.5\%$ (Eq. 4), and a QND-equivalent fidelity of $F_q \approx 77\%$. All of these results are obtained operating at a measurement efficiency of only $\eta \approx 0.1\%$, indicating orders-of-magnitude room for improvement in future devices that utilize nanophotonics. Finally, we use rapid microwave spin control and long spin coherence to study dephasing induced by measurement. This demonstrates the fundamental interplay between measurement and dephasing that is inherent to quantum mechanics. It is also a versatile technique to characterize how strongly a laser drive interacts with a qubit, and to characterize measurement efficiency.

Our work advances the SnV⁻ as a platform for building quantum networks. Taken together with other recent SnV⁻ work including nanophotonic integration [29, 30, 33, 34], microwave spin control [26, 27], spin-photon entanglement [31], and nuclear spin states [32, 36], the SnV⁻ has all the features necessary for building a quantum repeater node of similar scale and complexity to SiV⁻ based devices [15–17], but which favorably are robust to heating effects and elevated temperatures. More broadly, the understanding and methods we develop here – in particular the use of weak quantum measurement

and measurement induced dephasing – serve as powerful metrological tools and are applicable to the study of a wide variety of solid-state atom-like systems.

Acknowledgments.— This work has been supported by the Department of Energy under the Q-NEXT program, and Grant No. DE-SC0020115 and by the National Science Foundation Award ECCS 2150633. E.I.R. and C.P.A. acknowledge support by an appointment to the Intelligence Community Postdoctoral Research Fellowship Program at Stanford University administered by Oak Ridge Institute for Science and Education (ORISE) through an interagency agreement between the U.S. Department of Energy and the Office of the Director of National Intelligence (ODNI). J.C. acknowledges support from the Terman Faculty Fellowship at Stanford. H.C.K. acknowledges support by the Burt and Deedee McMurtry Stanford Graduate Fellowship (SGF). J.G. acknowledges support from the Hertz Fellowship. G.S. and S.A. acknowledge support from the Stanford Bloch Postdoctoral Fellowship. D.R. acknowledges support from the Swiss National Science Foundation (Project No. P400P2.194424). D.R. and S.A. contributed to this work prior to joining AWS. This work was performed, in part, at the Center for Integrated Nanotechnologies, an Office of Science User Facility operated for the U.S. Department of Energy (DOE) Office of Science. Sandia National Laboratories is a multimission laboratory managed and operated by National Technology & Engineering Solutions of Sandia, LLC, a wholly owned subsidiary of Honeywell International, Inc., for the U.S. DOE’s National Nuclear Security Administration under contract DE-NA-0003525. The views expressed in the article do not necessarily represent the views of the U.S. DOE or the United States Government. We thank Jacob Feder, Jonathan Marcks, Mia Froehling Gallier and Cyrus Zeledon for help with instrument control code, based on the “nspyre” framework [60]. We thank Haiyu Lu, Shuo Li, Patrick McQuade, Zhi-Xun Shen and Nicholas Melosh for assistance with diamond sample preparation. We thank Nazar Delgan and F. Joseph Heremans for collaboration on the preparation of related devices. Part of this work was performed at the Stanford Nanofabrication Facility (SNF) and the Stanford Nano Shared Facilities (SNSF), supported by the NSF under Grant No. ECCS-2026822.

Appendix A: Readout model

1. Dynamics of emission, polarization and dephasing

a. Three-level model

In this section we model the dynamics of an SnV^- center under a resonant drive. This will be used to model spin polarization, photon emission during readout, and measurement induced dephasing. Consider a three-level

system (a “ Λ -system”) consisting of two ground states $|\downarrow\rangle$ and $|\uparrow\rangle$, with an excited state $|A\rangle$, Fig. 6. This is a simplified version of the energy diagram in Fig. 2a. Relaxation from $|A\rangle$ occurs with probability P_{A1} or P_{A2} into the $|\downarrow\rangle$ or $|\uparrow\rangle$ states, respectively, and cyclicity $\chi = P_{A1}/P_{A2}$. Since $P_{A1} + P_{A2} = 1$ we have $P_{A2} = 1/(1 + \chi)$ and $P_{A1} = \chi/(1 + \chi)$.

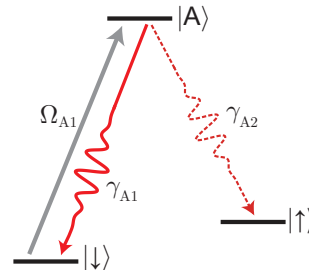


FIG. 6. A three-level atomic system is driven to the $|A\rangle$ state at rate Ω_{A1} . From $|A\rangle$, the system emits radiation via relaxation to the $|\downarrow\rangle$ state at rate γ_{A1} , or the $|\uparrow\rangle$ state at rate γ_{A2} .

We model this system using the master equation (setting $\hbar = 1$):

$$\frac{d}{dt}\hat{\rho} = -i[\hat{H}, \hat{\rho}] + \mathfrak{L}[\hat{\rho}], \quad (\text{A1})$$

$$\mathfrak{L}[\hat{\rho}] = \sum_{k=1}^2 \hat{L}_k \hat{\rho} \hat{L}_k^\dagger - \frac{1}{2}(\hat{L}_k^\dagger \hat{L}_k \hat{\rho} + \hat{\rho} \hat{L}_k^\dagger \hat{L}_k). \quad (\text{A2})$$

Here, $\hat{\rho}$ is the density matrix of the three-level system in Fig. 6, \hat{H} is the Hamiltonian, and $\hat{L}_k \in \{\hat{L}_1, \hat{L}_2\}$ are the stochastic quantum jump operators.

Under a Rabi drive the Hamiltonian in a rotating frame is:

$$\hat{H} = \frac{\Omega_{A1}}{2} \left(|\downarrow\rangle \langle A| + |A\rangle \langle \downarrow| \right) + \frac{\delta}{2} \left(|\downarrow\rangle \langle \downarrow| - |A\rangle \langle A| \right), \quad (\text{A3})$$

where the first term contains the optical Rabi rate Ω_{A1} , and the second term describes its detuning δ from the $A1$ transition. We also define stochastic quantum jump operators:

$$\hat{L}_1 = \sqrt{\gamma_{A1}} |\downarrow\rangle \langle A|, \quad (\text{A4})$$

$$\hat{L}_2 = \sqrt{\gamma_{A2}} |\uparrow\rangle \langle A|, \quad (\text{A5})$$

with $\gamma_{A1} = \gamma\chi/(1 + \chi)$ and $\gamma_{A2} = \gamma/(1 + \chi)$, and where $\gamma = \gamma_{A1} + \gamma_{A2}$ is the optical decay rate given by the lifetime of the $|A\rangle$ state.

b. Two-level model

This model can be simplified by considering only the subspace spanned by the spin levels $|\downarrow\rangle$ and $|\uparrow\rangle$. This obfuscates the coherent dynamics between the spin ground

states and the $|A\rangle$ state, but captures the effects of spin polarization and measurement-induced dephasing.

With this simplification, the master equation becomes $\frac{d}{dt}\hat{\rho} = \mathfrak{L}[\hat{\rho}]$ with operators:

$$\hat{L}_1 = \sqrt{R_1} |\downarrow\rangle \langle \downarrow|, \quad (\text{A6})$$

$$\hat{L}_2 = \sqrt{R_2} |\uparrow\rangle \langle \downarrow|, \quad (\text{A7})$$

only. Here, rates $R_1 = RP_{A1} = R\chi/(1+\chi)$ and $R_2 = RP_{A2} = R/(1+\chi)$ are:

$$R = \frac{\gamma}{2} \left(\frac{p/p_{\text{sat}}}{1 + p/p_{\text{sat}} + (\frac{\delta}{\gamma/2})^2} \right), \quad (\text{A8})$$

where $p/p_{\text{sat}} = 2\Omega_{A1}^2/\gamma^2$ is the resonant saturation parameter, which can be derived from the optical Bloch equations [41].

These dynamics have a clean analytical solution. When driven on the A1 transition, a qubit starting at time $t = 0$ in the state given by density matrix $\hat{\rho} = |\psi\rangle \langle \psi|$, with $|\psi\rangle = \alpha|\downarrow\rangle + \beta|\uparrow\rangle$ and $|\alpha|^2 + |\beta|^2 = 1$, will evolve as:

$$\rho_{\downarrow\downarrow}[t] = |\alpha|^2 e^{-\kappa t}, \quad (\text{A9})$$

$$\rho_{\uparrow\downarrow}[t] = \alpha\beta^* e^{-\Gamma_\phi t}, \quad (\text{A10})$$

$$\rho_{\downarrow\uparrow}[t] = \alpha^*\beta e^{-\Gamma_\phi t}, \quad (\text{A11})$$

$$\rho_{\uparrow\uparrow}[t] = 1 + (|\beta|^2 - 1)e^{-\kappa t}, \quad (\text{A12})$$

where $\Gamma_\phi = R/2$ and $\kappa = R/(1+\chi)$. The qubit therefore undergoes drive-induced dephasing at rate Γ_ϕ , and polarization at the slower rate κ .

c. Comparison between models

To confirm these models, we compare simulations of the three-level model in Sec. A 1 a to the two-level model in Sec. A 1 b. In each case, we numerically solve the master equation using the QuTiP package [61].

The time-domain dynamics of both models are plotted in Fig. 7. In both cases the system undergoes spin polarization at rate κ and an overall envelope of drive-induced dephasing at rate Γ_ϕ . The three-level model also captures the coherent dynamics between the spin ground states and the $|A\rangle$ state. We simulate both models as a function of detuning δ , and confirm they match. This comparison also illustrates power broadening – the effective increase in linewidth at high drive powers.

2. Emission model

A driven atomic system emits at the steady-state photon scattering rate given by Eq. A8, times the population in the driven spin state [41]. For example, upon onset of a laser drive at time $t = 0$ the emission rate is:

$$\Gamma_{\text{em}}(t) = |\alpha|^2 R e^{-\kappa t}, \quad (\text{A13})$$

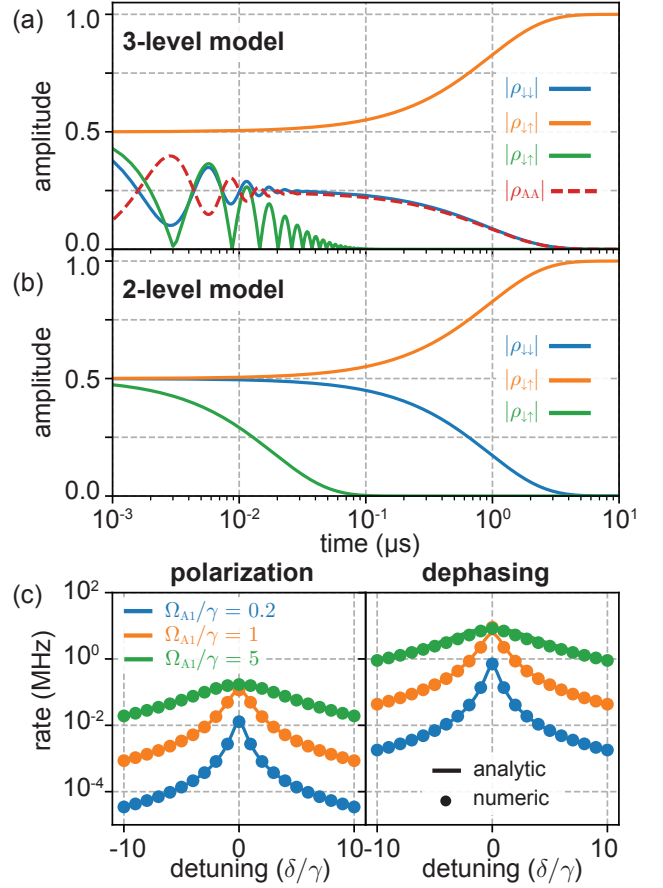


FIG. 7. (a) Dynamics of a driven 3-level atomic system, Fig. 6, simulated using the Hamiltonian and collapse operators given by Eq. A3-A5. (b) Dynamics of the simplified 2-level model, simulated using collapse operators Eq. A6 and Eq. A7. Both (a) and (b) use $\chi = 100$, $\gamma/2\pi = 35$ MHz, $\Omega_{A1} = 5\gamma$, and $\delta = 0$. (c) Polarization rate κ (left) and dephasing rate Γ_ϕ (right) as functions of δ , and at different values of Ω_{A1}/γ . Numerical solutions to the 3-level model described in Appendix A 1 a (dots) match the analytical solutions (Eq. A9-Eq. A12) based on the 2-level model in Appendix A 1 b (lines).

where $|\alpha|^2$ is the initial population in the $|\downarrow\rangle$ state. We now use this rate to model readout.

In readout, “dark” or “bright” distributions with low (\bar{n}_d) or high (\bar{n}_b) mean photon numbers are associated with the qubit being prepared in different spin states prior to measurement. For example, state preparation of $|\uparrow\rangle$ yields $\alpha = 0$, no initial emission, and a dark collected distribution. State preparation of $|\downarrow\rangle$ yields $\alpha = 1$, maximum initial emission, and a bright collected distribution. However, emitted photons are only collected with a probability η (the measurement efficiency) and furthermore, collected counts can also come from unwanted sources unrelated to the qubit, i.e. noise arriving at rate Γ_{noise} .

We therefore model \bar{n}_d and \bar{n}_b as:

$$\bar{n}_d = \int_0^\tau \Gamma_{\text{noise}} dt, \quad (\text{A14})$$

$$\bar{n}_b = \int_0^\tau (\Gamma_{\text{noise}} + \eta\Gamma_{\text{em}}) dt, \quad (\text{A15})$$

where τ is the readout integration window. We model noise to be time-independent arriving at rate $\Gamma_{\text{noise}} = a + bp$, where a is the mean rate of background noise photons including dark counts, b is noise from scatter of the excitation laser into the collection path and is proportional to power. We fit this data to Eq. A14 to determine $a\tau = 0.028 \pm 0.002$ photons and $b\tau = (6.24 \pm 0.15) \times 10^{-5}$ photons/nW.

For preparation in the spin state associated with maximum emission ($\alpha = 1$), the difference in collected counts between the bright and dark distributions is therefore: $\bar{n}_b - \bar{n}_d = \eta\chi(1 - e^{-\kappa\tau})$. For $\kappa\tau \gg 1$, so the duration of drive is long enough to entirely polarize the spin state, this reduces to $\bar{n}_b - \bar{n}_d = \eta(\chi+1)$. In other words, the expected number of detection events is essentially the cyclicity χ times the measurement efficiency η .

3. Readout fidelity vs. power

We now use this model of emission to study readout fidelity as a function of power. Readout fidelity quantifies the distinction between the “bright” or “dark” distributions of photons collected when the qubit is prepared in the $|\downarrow\rangle$ or $|\uparrow\rangle$ spin state. These distributions are distinguished by a readout threshold N_r , meaning the outcome “0” can be associated with the collection of $\geq N_r$ counts per readout window, and the outcome “1” with $< N_r$ counts. In practice, N_r is chosen to maximize readout fidelity $F_r = 1 - \frac{1}{2}P(1|\downarrow) - \frac{1}{2}P(0|\uparrow) = \frac{1}{2}P(0|\downarrow) + \frac{1}{2}P(1|\uparrow)$.

Here, $P(1|\downarrow)$ and $P(0|\uparrow)$ are error probabilities, associated with the chance a collected number of counts falls within a different distribution than expected given state preparation. Infidelity can result from too many counts in the dark distribution or too few counts in the bright distribution. It can also result from state preparation errors ϵ_1 (ϵ_0); the chances the qubit was actually prepared in the $|\downarrow\rangle$ ($|\uparrow\rangle$) state when it was attempted to be prepared in the $|\uparrow\rangle$ ($|\downarrow\rangle$) state, respectively.

To model readout fidelity we assume that emission follows Poissonian statistics arising from a Markovian process. These statistics are known to describe emission from atomic systems [62], but can be modified in other experiments where interaction with a photonic structure changes the electromagnetic density of states [33]. Poissonian statistics are captured by the model in Eq. A1, which leads to the emission rate in Eq. A13. Therefore during a readout event, collection of k counts is expected with probability:

$$p[k, n] = \frac{n^k e^{-n}}{k!}, \quad (\text{A16})$$

where $n = \bar{n}_b$ ($n = \bar{n}_d$) for readout associated with preparation in the spin state that results in the bright (dark) distribution.

The error probabilities $P(1|\downarrow)$ and $P(0|\uparrow)$ are thus:

$$P(1|\downarrow) = \sum_{k=0}^{N_r-1} (1 - \epsilon_0)p[k, \bar{n}_b] + \epsilon_0 p[k, \bar{n}_d], \quad (\text{A17})$$

$$P(0|\uparrow) = \sum_{k=N_r}^{\infty} \epsilon_1 p[k, \bar{n}_b] + (1 - \epsilon_1)p[k, \bar{n}_d]. \quad (\text{A18})$$

Evaluating using the statistics given by Eq. A16 yields:

$$F_r = \frac{1}{2} + \frac{f_0}{2} \left(\frac{\Gamma[N_r, \bar{n}_d] - \Gamma[N_r, \bar{n}_b]}{\Gamma[N_r, 0]} \right), \quad (\text{A19})$$

where $\Gamma[N_r, n] = \int_n^\infty t^{N_r-1} e^{-t} dt$ is the Gamma function and $f_0 = 1 - \epsilon_0 - \epsilon_1$ sets the maximum attainable readout fidelity. This can be simplified if $N_r = 1$, a choice which optimizes readout fidelity for all measurements in this work. Doing so yields:

$$F_r = \frac{1}{2} + \frac{f_0}{2} (e^{-\bar{n}_d} - e^{-\bar{n}_b}). \quad (\text{A20})$$

Appendix B: Extended discussion

1. Understanding the SnV⁻ Hamiltonian

The SnV⁻ Hamiltonian is predicted by *ab initio* calculations in Ref. [40]. In our previous work, Ref. [26], these calculations are compared to experimental values obtained by fitting the eigenvalues of the SnV⁻ Hamiltonian to measurement of its level structure vs. magnetic field orientation. There are many parameters in this fit including strain, spin-orbit coupling, the orbital Zeeman effect, anisotropy of the Zeeman effect, and the vector orientation of the spin dipole. This fit is under-determined if every parameter of the SnV⁻ Hamiltonian is taken as a free parameter, and so to constrain the fit we made assumptions: (1) The direction normal to the surface of the chip is parallel to the \hat{z} -axis of the magnetic coil. (2) The magnet calibration is accurate and magnet hysteresis is negligible. (3) Higher order terms in the SnV⁻ Hamiltonian are neglected [40].

The values of the SnV⁻ Hamiltonian reported in Table 1 of Ref. [26] rely on these assumptions, which are imperfect at some level. While this analysis was a more precise determination of the SnV⁻ Hamiltonian than prior experimental work [20–23], it can be improved upon by future experiments that do not rely on these assumptions. For example, subsequent work in Ref. [24] reports slightly different values of the SnV⁻ Hamiltonian but constrains the fit by studying multiple emitters, by using a three-axis vector magnet to optimize alignment with the spin dipole, and by quantifying the magnet’s calibration.

2. Estimating angular misalignment

Understanding the SnV^- Hamiltonian helps to understand spin polarization and readout, including by determining alignment between the magnetic field and spin dipole moment. In our current experiment we use a two-axis vector magnet, only, which prohibits arbitrary alignment between the magnet and spin. To estimate the minimum misalignment we compare the measurement of cyclicity vs. ζ (Fig. 2e) to a model based on the driven SnV^- Hamiltonian (see Appendix B.3 of Ref. [26]), and using the Hamiltonian parameters from Ref. [24]. This model closely follows our data for an azimuthal misalignment of $\varphi \approx 10^\circ$. Use of the alternate Hamiltonian parameters reported in Ref. [26] has minimal effect on this result.

3. Comparison to prior work

Despite subtleties in determining the SnV^- Hamiltonian and angular misalignment, it is clear that the readout fidelity reported in this work uses an SnV^- center which is only somewhat aligned with the external \vec{B} field, has a spin polarization time of $\approx 20 \mu\text{s}$, and has a cyclicity of $\approx 2 \times 10^3$. At this operating condition we achieve single shot readout of the SnV^- center's electronic spin with an average of up to ≈ 4 photons collected during a $50 \mu\text{s}$ integration window. In Table I, we compare these results to prior examples of single-shot spin readout of color centers in diamond.

Looking to the future, the misalignment and modest collection efficiency of our experiment emphasize how much SnV^- readout can be improved. Even with these non-idealities, the rate of photon collection in our work is much greater than that in the first demonstration of single-shot readout of an SiV^- electron spin [12], which reported an average of ≈ 6 photons collected during a 20 ms readout window. This may reflect the SnV^- 's higher quantum efficiency, η_q : Ref. [40] calculates $\eta_q = 0.14$ for the SiV^- and $\eta_q = 0.91$ for the SnV^- . Subsequent work on SiV^- readout has shown greater collection efficiency over faster timescales by optimized use of nanophotonics [15–17]. Our results here suggest such improvement will also be possible using the SnV^- .

We also compare our results to Ref. [39], to our knowledge the only prior published single-shot readout of an SnV^- electronic spin. Ref. [39] demonstrates readout of 74% fidelity (max of 1.2 mean counts per shot) collected during a $200 \mu\text{s}$ readout window. This result is achieved in a bulk sample on an unstrained SnV^- . Lack of strain yields high-cyclicity with reduced sensitivity to alignment of the magnetic field, but also suppresses the magnetic dipole transition necessary for spin control [26]. Finally, we note that Ref. [32] measures single-shot readout of a nuclear spin via a waveguide-integrated SnV^- , obtaining a single-shot nuclear spin readout fidelity of 80% in $15 \mu\text{s}$. In comparison, our work demonstrates a regime in

which *both* single-shot readout of an SnV^- 's electronic spin, and, rapid microwave control of this spin are possible.

Finally, readout fidelity can be boosted by performing spin-to-charge conversion [63]. We have already demonstrated charge state readout with our CRC check. A spin-dependent ionization process could be achieved with a narrow line, spin-selective laser and a high power ionization laser. Combined, they could provide increased photons measured per shot, separating the bright and dark histograms and boosting fidelity.

Appendix C: Experimental details

1. Setup

The setup used in this experiment, Fig. 8, is similar to that in Ref. [26] but optimized for higher transmission on the collection path. The repump (532 nm) and resonant (M-Squared) lasers are both modulated by acousto-optic modulator (4C2C-532-AOM and 4C2C-633-AOM, Gooch and Housego). Typically, we operate with the excitation laser detuned by several GHz from the SnV^- 's optical transitions, and drive these transitions using the first sideband created by an electro-optic modulator (PM-0S5-PFU-PFU-620, Eospace). By combining two microwave signal generators (SG396, SRS) using a microwave power combiner, we can drive the A1 transition only, the B2 transition only, or both simultaneously as is necessary for implementing charge resonance checks. Pulsing is controlled by an arbitrary waveform generator (Pulse Streamer 8/2, Swabian).

For spin control, microwaves are delivered by a wire-bond draped over the diamond chip as in Ref. [26], and using a similar microwave power (48 dBm into the cryostat). The wire-bond has been replaced from that used in Ref. [26]; we attribute the slower Rabi rate here to the new wire-bond simply being further from the spin.

To focus excitation light and collect signal confocally, a cryogenic objective (LT-APO/VISIR/0.82, Attocube) is placed directly above the chip. This objective has a focal length of 2.87 mm, a numerical aperture of 0.82, and a working distance of 0.65 mm. Signal is then routed out of the cryostat to a 90:10 beamsplitter, whose 90% port leads to a free-space to fiber coupler. This coupler is connected by a multimode optical fiber (FG025LJA, core diameter $25 \pm 3 \mu\text{m}$, Thorlabs) to a single photon counting module (SPCM-AQR-15-FC, Perkins Elmer). Detection events are time-tagged (PicoHarp300, PicoQuant).

Before the fiber coupler we place a 635 nm long pass filter (635 nm Longwave EdgeBasic, Semrock) to collect the SnV^- 's phonon sideband (PSB), only, thus filtering most excitation scatter and also the SnV^- 's zero-phonon line. Note that this wavelength still filters a fraction of the PSB; a different filter closer to the zero phonon line would have lead to greater counts, e.g. a filter at 625 nm. Finally, a 532 nm notch filter (532 nm StopLine,

TABLE I. Comparison to selected prior work on single-shot readout of color centers in diamond.

Reference	Qubit	fidelity, F_r	counts, \bar{n}_b	duration, τ	Device	Spin Control?
Robledo <i>et al.</i> [42]	NV ⁻	93%	6.4	40 μ s	SIL	Yes
Sukachev <i>et al.</i> [12]	SiV ⁻	89%	6.2	20 ms	Bulk	Yes
Gorlitz <i>et al.</i> [39]	SnV ⁻	74%	1.2	200 μ s	Bulk	No
Parker <i>et al.</i> [32]	SnV ⁻ (nuclear)	80%	1.6	15 μ s	Waveguide	No
This work	SnV ⁻	87.4%	4.3	50 μ s	Mesa	Yes

Semrock) is also placed on the collection path to mitigate noise from the repump laser; even though this laser is toggled off during readout, there is some non-zero feed through of the AOM used to toggle the green laser which can scatter into the collection path, and so this notch filter is still useful.

2. Sources of loss

In Table II, we estimate the sources of inefficiency and optical loss expected for this work. Multiplying all sources of inefficiency yields: $\eta = \eta_q \eta_{\text{psb}} \eta_{\text{phot}} \eta_{\text{col}} \eta_{\text{det}} \approx 0.4\%$. This qualitatively matches the measured values of $\eta \approx 0.2\%$ (Fig. 3) and $\eta \approx 0.1\%$ (Fig. 4).

The dominant source of loss is internal reflection of light into the diamond sample, Fig. 9. By fine tuning the emitter position using piezoelectric nanopositioners, we find this emitter to actually be in a mesa structure, rather than a nanopillar as stated in Ref. [26]. For an SnV⁻ center implanted at a depth of 100 nm and for structures 1 μ m in height, simulations determine scattering from bulk diamond to be $\approx 3\%$, scattering from a mesa is $\approx 5\% - 9\%$, Fig. 9d, and scattering from a pillar is $\approx 7\% - 28\%$, Fig. 9e. These values are reported at 645 nm, near the maximum of the SnV⁻'s phonon sideband (PSB). Given the proximity of the color center to a pillar, we use values for an SnV⁻ at the edge of the mesa structure and estimate the (average across the entire PSB) fraction $\eta_{\text{phot}} \approx 5\%$ of emitted light is scattered into our collection path. This number accounts for the modal mismatch between the far field for the SnV⁻ emission and the Gaussian mode accepted by the cryo-objective.

Other sources of loss include the emitter's quantum efficiency (the probability of non-radiative decay), filtering of the SnV⁻'s ZPL, loss in the optical path, and detector inefficiency. Finally, Table II may not capture every source of loss. Note that we use a 635 nm long pass filter to collect the PSB (see Appendix C 1 for details); this removes $\approx 14.5\%$ of the PSB light, and a cutoff of ≈ 624 nm would be best to avoid extra loss [20–23]. Additionally, while we use multi-mode fiber to maximize photon collection, some imperfection in the coupling could still be present.

Optimized diamond nanophotonics provides a clear path toward high improvement in collection efficiency (e.g. $\approx 25\%$ for inverse-designed grating couplers [49],

and $\approx 90\%$ for tapered fibers combined with 1D photonic crystal cavities [50]). These devices have also been demonstrated in conjunction with stable SnV⁻'s [28–30, 32–34]. The other sources of loss can be improved upon too. For example, loss associated with filtering of the resonant excitation laser can be avoided by filtering by polarization rather than by wavelength (routinely done in the form of cross-polarization detection). Optical loss in the collection path can be mitigated with higher quality optics, e.g. by using higher reflectivity mirrors, and by replacing the 90:10 beamsplitter on the collection path with a more transmissive component. Detector inefficiency can be improved by switching to state-of-the-art superconducting detectors.

With improved nanophotonics only, we expect a collection efficiency of order $\times 10$ or more, and with all possible improvements we expect an efficiency of order $\times 100$ or more can be achieved in future experiments. Even modest improvements in efficiency will allow for much higher single-shot readout fidelity (since fidelity is non-linear with number of photons), operation at lower drive power (see Fig. 4c), faster readout, and, single-shot readout at external magnetic fields with greater misalignment.

3. Extended data

a. Readout fidelity vs. power

Studying the power dependence of readout is important for the optimization of fidelity. Notice in Fig. 4b that while the number of signal photons $\bar{n}_b - \bar{n}_d$ plateaus near saturation, the total number of collected photons continues to increase with power. We attribute this rise to scatter of the excitation laser into the collection path (see Appendix A 1 for details).

This power dependence makes clear that readout fidelity can be optimized by operating near saturation. Below saturation, increasing power simply produces more signal. Above saturation, however, driving with more power does not increase signal and can only cause rising noise. To test this intuition, we plot readout fidelity vs. power in Fig. 10, measured from the same dataset used to produce Fig. 4b. Data are fit to the model in Eq. A20. This model assumes that emitted photons follow Poissonian statistics; see Appendix A 1 for a derivation.

Note that this fit uses $p_{\text{sat}} = 313$ nW and $\eta =$

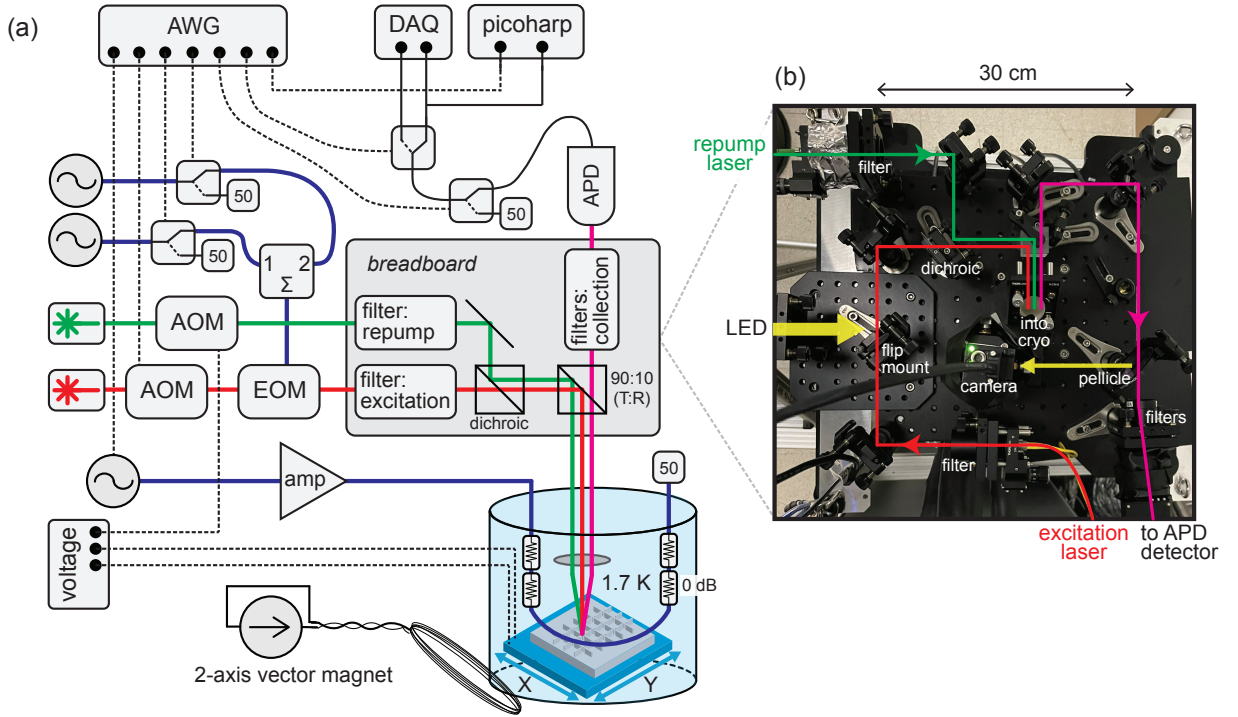


FIG. 8. (a) Experimental schematic. (b) Photograph of the optical breadboard.

TABLE II. Estimated sources of loss.

Source	Efficiency	Reference / Method	Path to Improve
Quantum efficiency: η_q	80% – 90%	[20, 40]	
Debye-Waller factor: η_{psb}	43%	[23]	resonant collection (cross-polarization)
Scattering from chip: η_{phot}	5%	simulation, Fig. 9	nanopillars, waveguides, cavity-QED
Optical path loss: η_{path}	35%	transmission, at 670 nm	optimized optics
Detector: η_{det}	65%	datasheet spec., at 650 nm	superconducting detectors
Total: η	0.4%	$\eta = \eta_q \eta_{psb} \eta_{phot} \eta_{path} \eta_{det}$	all of the above

0.992×10^{-3} obtained from fits to Fig. 4b, and fits for $f_0 = 0.89 \pm 0.032$ and $\chi = 977 \pm 72$ as free parameters. Fixing $\chi = 2244$ as a fixed parameter, as expected from the data in Fig. 2, does not produce a fit which closely matches the data in Fig. 4b. This discrepancy could be attributed to non-Poissonian statistics of light emitted from the SnV^- (an assumption of Eq. A20), and/or, from detrimental effects due to SnV^- instability (e.g. cycles where the CRC is passed, but a blinking event occurs before or during the readout step). As such, the models in Eq. 6 and Eq. A20 should be taken as simplifications that do not capture every possible effect on readout of the system, and the parameters reported from these fits should be taken as estimates based on these simplified assumptions, only.

b. Charge resonance checks

The readout characterization experiment in Fig. 3 includes charge resonance checks (CRCs) applied at both the beginning and end of each characterization cycle. A CRC consists of driving both the A1 and B2 transitions while simultaneously collecting emission. Many photons are collected during the CRC if the excitation is indeed resonant (e.g. neither the laser nor transition frequencies have drifted), and, the system has not left the qubit subspace (e.g. it has not “blinking off”).

The distribution of counts collected during a CRC are shown in Fig. 12a, using data from the “wfm-A” experiment in Fig. 3. Data from wfm-B are nearly identical. The CRC result is recorded as a “pass” if $\geq N_c$ counts are measured and a “fail” if $< N_c$ counts are measured, where N_c is the CRC discrimination threshold. Choosing $N_c = 30$ for both CRCs for the data in Fig. 3, we find that 7.4% of cycles of wfm-A pass both CRC’s, and 7.7%

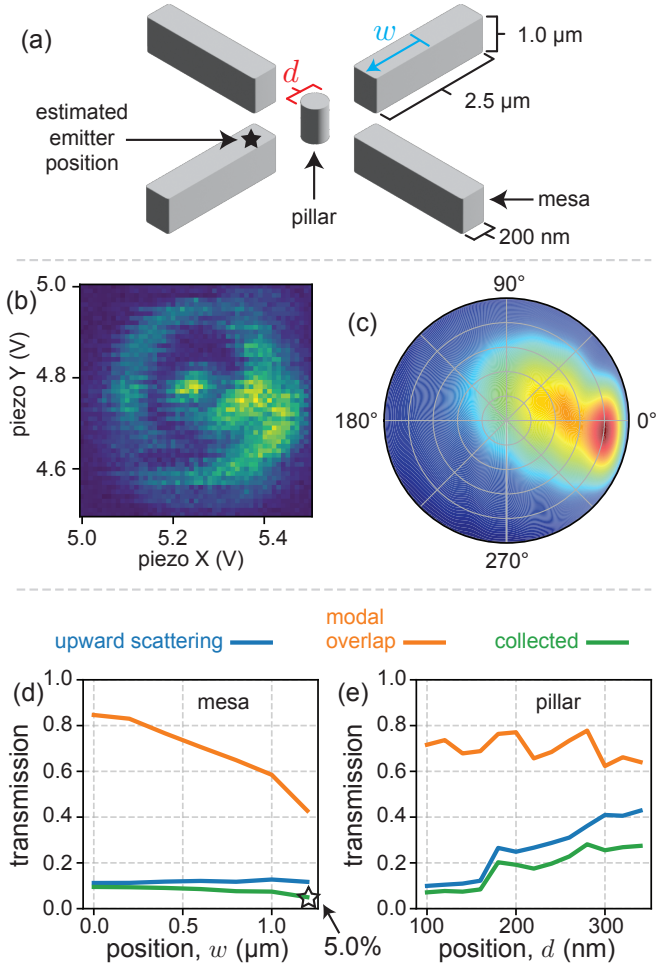


FIG. 9. (a) Device. The $\langle 100 \rangle$ diamond chip contains arrays of nanophotonic structures, both pillars and mesas. Structures have a height of $1 \mu\text{m}$ and Sn atoms are implanted at a depth of $\approx 90 \pm 20 \text{ nm}$ [26]. (b) Scan to optimize focal position. The center of the measured lobe (which originates from imaging with a multi-mode fiber under slightly de-focused conditions) corresponds to focal alignment at the edge of a mesa. A scan range of 0.2 V corresponds to a lateral distance of $\approx 1 \mu\text{m}$. (c) Numerical simulation of the far-field scattering pattern from an SnV^- center in a mesa. (d) Numerical simulation of 645 nm light collected from both a mesa and (e) a pillar. Simulations include the fraction of light scattered upward, the modal overlap of the objective and the scattering pattern, and their product which gives the overall fraction of light routed to the collection path. From the simulation in (d) we conclude $\eta_{\text{phot}} \approx 5\%$ of emission enters the collection path. In comparison, similar simulations show a scattering efficiency of 3% from an emitter in bulk diamond at a depth of 100 nm .

of cycles for wfm-B pass both CRC's, out of 4.27×10^5 cycles total for each waveform.

The probability that consecutive cycles pass either the first or second check is plotted in Fig. 12b, using a pass threshold of $N_c = 8$ (the inflection threshold between the dark and bright distributions, Fig. 12a). This probabil-

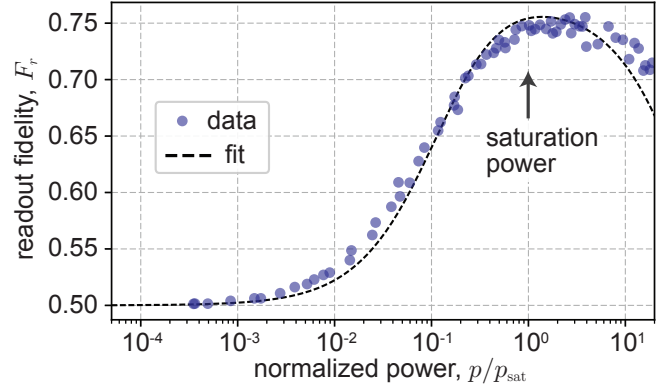


FIG. 10. Readout fidelity vs. power. Data is fit to Eq. A20.

ity decays exponentially, consistent with fail events occurring at random. However, probability falls faster for the second check, which may result from drive-induced blinking [35].

c. Coherence time

The qubit's coherence time is measured using a CPMG-2 pulse sequence [64], Fig. 14, operating at $|\vec{B}| = 125 \text{ mT}$ and $\zeta = 147^\circ$. We measure a spin coherence time of $T_2^{\text{CPMG-2}} = 270 \pm 30 \mu\text{s}$ using a CPMG-2 dynamical decoupling sequence [64]. This measurement is comparable to results in Ref. [26], which operate at $\chi \approx 80$. For spin-1/2 group-IV qubits, at some magnetic field orientations dynamical decoupling has limited effect because the qubit's g -factor is too similar to the predominantly spin-1/2 bath [26]. The measurement in Fig. 14 shows that here we avoid this detrimental effect.

d. Quantum jumps

We take advantage of single-shot readout to observe real time quantum jumps of the electron spin [42]. The protocol, illustrated in Fig. 15a, consists of a green repump, then spin polarization, followed by readout on the same state that was polarized in the presence of a weak microwave drive. During this readout step, time-tagged photon detection events are binned into $10 \mu\text{s}$ windows and plotted as a time trace in Fig. 15b. In the absence of the weak spin drive we expect ≈ 0 photons due to high-fidelity initialization of the spin state and thus a complete dark time-trace of the collected fluorescence. However, the weak spin drive (microwave power $\approx 1 \text{ dBm}$ at the sample) occasionally kicks the spin-state from $|\uparrow\rangle$ to $|\downarrow\rangle$ - for example when initialized using the A1 transition. This results in photons being emitted which can be seen as discrete spikes in the time-trace as our readout determines the state in $|\downarrow\rangle$. Using a photon threshold

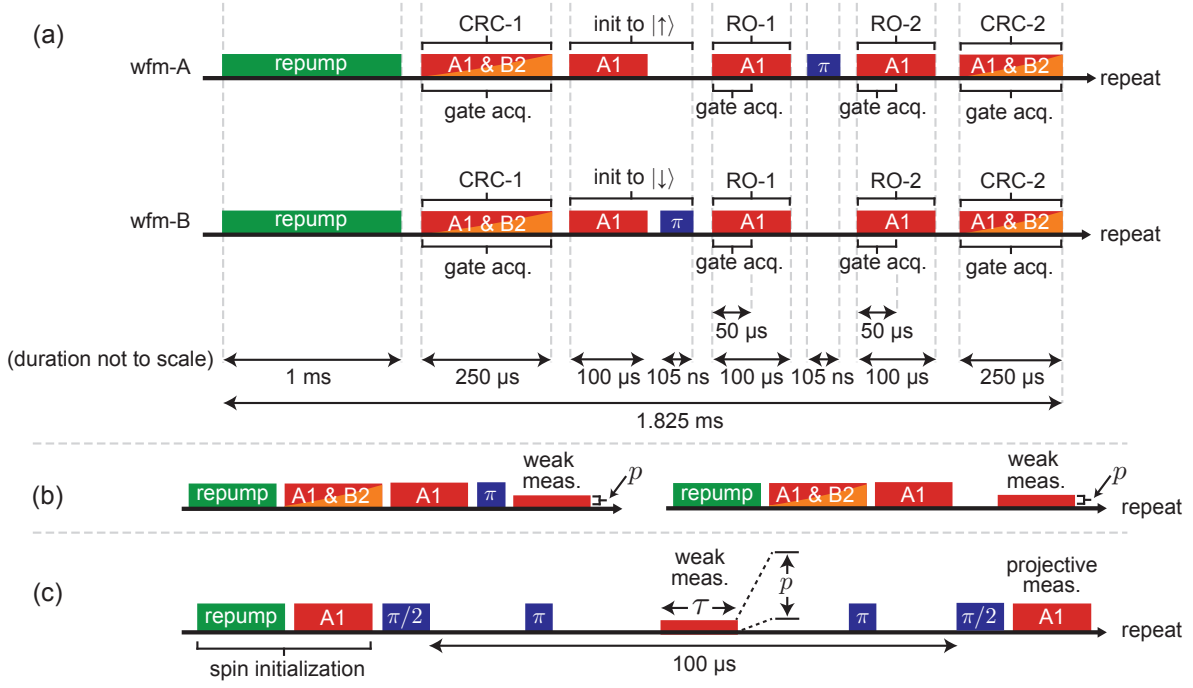


FIG. 11. Timing diagrams of the experiments in: (a) Fig. 3, (b) Fig. 4b, (c) Fig. 5. Illustrations are not to scale. Steps are generally separated by 2μ s pauses (not shown). Weak measurement pulses in (b) and (c) resonantly drive the A1 transition, as in the spin polarization and projective measurement steps.

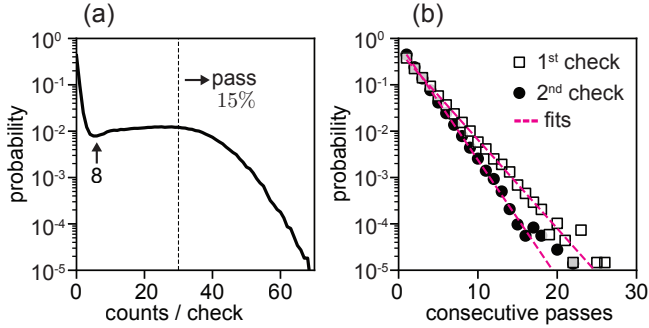


FIG. 12. (a) Distribution of counts collected during the charge resonance checks (CRCs) in Fig. 3. Each CRC consists of simultaneously driving the A1/B2 transitions. Separate distributions with few or many counts per check are separated by an inflection point around 8 counts. Choosing a pass threshold of $N_c = 30$ leads to $\approx 15\%$ cycles passing the first check, and of these, $\approx 50\%$ pass the second check. (b) Probability of consecutive passes before a fail is recorded, using $N_c = 8$. Data are fit to exponential decay. Faster decay is observed for the second check, likely due to drive-induced charging in the intervening readout steps. In both panels only data from wfm-A is plotted; data for wfm-B is nearly identical.

of $N_r \geq 2$ (black dashed line), we distinguish between the “bright” and “dark” state and denote the electron being in the $|\uparrow\rangle(|\downarrow\rangle)$ state. Optical re-initialization also happens naturally under the continuous pump, so the jumping between the spin states (bright and dark) is a mixture of bidirectional mixing (microwave) and one-way reinitialization (bright to dark). To ensure capturing the quantum jumps is not convoluted with charge or spectral hopping, the entire sequence is bracketed with CRCs before and after each measurement shot (using a photon threshold of $N_c = 30$ for both CRCs). In this experiment, the spin flip process from T_1 (order Hz at the 1.7 Kelvin sample temperature [26, 27]) is much slower than the readout process. For clarity, Fig. 15c shows the same time trace where the electronic state is assigned as “0” or “1”, based on the discrimination threshold (N_r).

4. List of data

In Table III we provide a summary of data and operating conditions.

[1] H. J. Kimble, Nature **453**, 1023–1030 (2008).

[2] C. Bradac, W. Gao, J. Forneris, M. E. Trusheim, and I. Aharonovich, Nat. Comm. **10**, 5625 (2019).

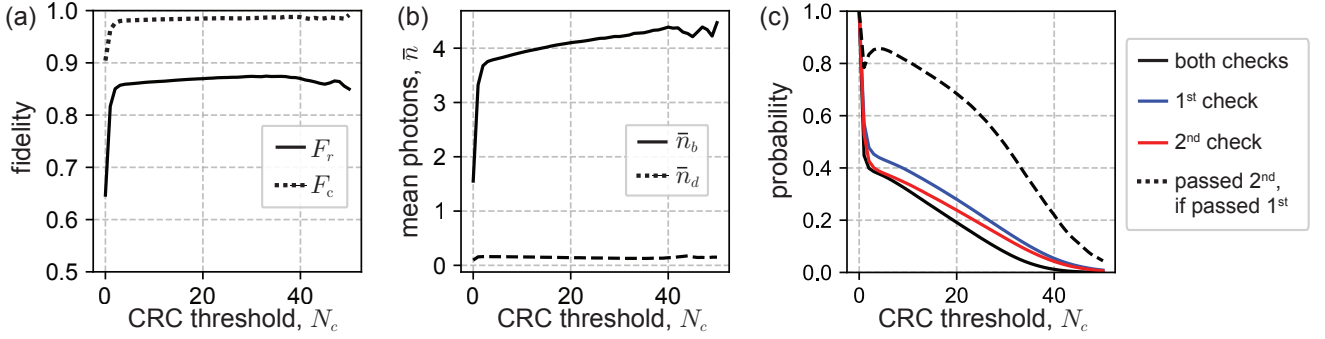


FIG. 13. Analysis of the time tagged dataset shown in Fig. 3, as a function of charge resonance check (CRC) threshold photon number N_c . If both CRCs per cycle each produce a photon number $\geq N_c$, the readout steps in that cycle are kept for analysis. (a) Readout fidelity F_r , and conditional fidelity F_c (first readout step and wfm-A, respectively; results from the second readout step and wfm-B look nearly identical). (b) Mean photon number in the bright and dark distributions (first readout step; results from the second step look nearly identical). (c) Probability of passing each CRC, both CRCs, and the probability of the second CRC given a pass of the first. (Data is from wfm-A; results from wfm-B look nearly identical.)

TABLE III. Summary of data and operating conditions. Repump power is typically order $100 \mu\text{W}$ and resonant excitation power is typically order $1 - 10 \mu\text{W}$, both specified going into the cryostat. Note that in all data the qubit is driven with the first sideband of the laser created by an electro-optical modulator, not the carrier signal.

Data	Figure	Magnet: amplitude $ \vec{B} $	Magnet: angle ζ	Repump duration	Init. duration	Readout duration	Cycle time	CRC?
Transitions vs. ζ	Fig. 2c	180 mT	swept	$1 \mu\text{s}$		$1 \mu\text{s}$	$22 \mu\text{s}$	no
Spin polarization	Fig. 2d	180 mT	53° and 147°	$100 \mu\text{s}$	$100 \mu\text{s}$		$202 \mu\text{s}$	no
Cyclicity vs. ζ	Fig. 2e	180 mT	swept	$100 \mu\text{s}$	$100 \mu\text{s}$		$202 \mu\text{s}$	no
Rabi	Fig. 2f	125 mT	147°	$500 \mu\text{s}$	$100 \mu\text{s}$	$100 \mu\text{s}$	$719 \mu\text{s}$	no
Rabi vs. ζ	Fig. 2g	132-183 mT	147°	$20 - 500 \mu\text{s}$	$5 - 120 \mu\text{s}$	$1 - 60 \mu\text{s}$	$44 - 679 \mu\text{s}$	no
Single-shot readout	Fig. 3	125 mT	147°	$1000 \mu\text{s}$	$100 \mu\text{s}$	$50 \mu\text{s}$	$1825 \mu\text{s}$	yes
Emission vs. p/p_{sat}	Fig. 4	125 mT	147°	$500 \mu\text{s}$	$100 \mu\text{s}$	$70 \mu\text{s}$	$1825 \mu\text{s}$	yes
Dephasing	Fig. 5	125 mT	147°	$500 \mu\text{s}$	$100 \mu\text{s}$	$70 \mu\text{s}$	$1552 \mu\text{s}$	no
Scattering pattern	Fig. 9a	180 mT	125°	$10 \mu\text{s}$		$10 \mu\text{s}$	$122 \mu\text{s}$	no
F_r vs. p/p_{sat}	Fig. 10	125 mT	147°	$500 \mu\text{s}$	$100 \mu\text{s}$	$70 \mu\text{s}$	$1825 \mu\text{s}$	yes
CRC statistics	Fig. 12	125 mT	147°	$1000 \mu\text{s}$	$100 \mu\text{s}$	$50 \mu\text{s}$	$1825 \mu\text{s}$	yes
F_r vs. N_c	Fig. 13	125 mT	147°	$1000 \mu\text{s}$	$100 \mu\text{s}$	$50 \mu\text{s}$	$1825 \mu\text{s}$	yes
CPMG-2	Fig. 14	125 mT	147°	$500 \mu\text{s}$	$100 \mu\text{s}$	$80 \mu\text{s}$	$3174 \mu\text{s}$	no
Quantum jumps	Fig. 15	125 mT	147°	$500 \mu\text{s}$	$200 \mu\text{s}$	$1000 \mu\text{s}$	$2123 \mu\text{s}$	yes

- [3] E. Janitz, M. K. Bhaskar, and L. Childress, *Optica* **7**, 1232 (2020).
- [4] G. Wolfowicz, F. J. Heremans, C. P. Anderson, S. Kanai, H. Seo, A. Gali, G. Galli, and D. D. Awschalom, *Nature Review Materials* **6**, 906–925 (2021).
- [5] S. Wehner, D. Elkouss, and R. Hanson, *Science* **362**, 6412 (2018).
- [6] M. Pompili, S. L. N. Hermans, S. Baier, H. K. C. Beukers, P. C. Humphreys, R. N. Schouten, R. F. L. Vermeulen, M. J. Tiggelman, L. Dos Santos Martins, B. Dirkse, S. Wehner, and R. Hanson, *Science* **372**, 259–264 (2021).
- [7] S. L. N. Hermans, M. Pompili, H. K. C. Beukers, S. Baier, J. Borregaard, and R. Hanson, *Nature* **605**, 663–668 (2022).
- [8] S. Ourari, L. Dusanowski, S. P. Horvath, M. T. Uysal, C. M. Phenice, P. Stevenson, M. Raha, S. Chen, R. J. Cava, N. P. de Leon, and J. D. Thompson, *Nature* **620**, 977–981 (2023).
- [9] A. Ruskuc, C.-J. Wu, E. Green, S. L. N. Hermans, J. Choi, and A. Faraon, <https://arxiv.org/abs/2402.16224> (2024).
- [10] D. M. Lukin, M. A. Guidry, and J. Vučković, *PRX Quantum* **1**, 020102 (2020).
- [11] C. Hepp, T. Müller, V. Waselowski, J. N. Becker, B. Pingault, H. Sternschulte, D. Steinmüller-Nethl, A. Gali, J. R. Maze, M. Atatüre, and C. Becher, *Phys. Rev. Lett.* **112**, 036405 (2014).
- [12] D. D. Sukachev, A. Sipahigil, C. T. Nguyen, M. K. Bhaskar, R. E. Evans, F. Jelezko, and M. D. Lukin, *Phys. Rev. Lett.* **119**, 223602 (2017).
- [13] J. L. Zhang, S. Sun, M. J. Burek, C. Dory, Y.-K. Tzeng, K. A. Fischer, Y. Kelaita, K. G. Lagoudakis, M. Radulaski, Z.-X. Shen, N. A. Melosh, S. Chu, M. Lončar, and J. Vučković, *Nano Lett.* **18**, 1360–1365 (2018).
- [14] S. Sun, J. L. Zhang, K. A. Fischer, M. J. Burek, C. Dory, K. G. Lagoudakis, Y.-K. Tzeng, M. Radulaski, Y. Ke-

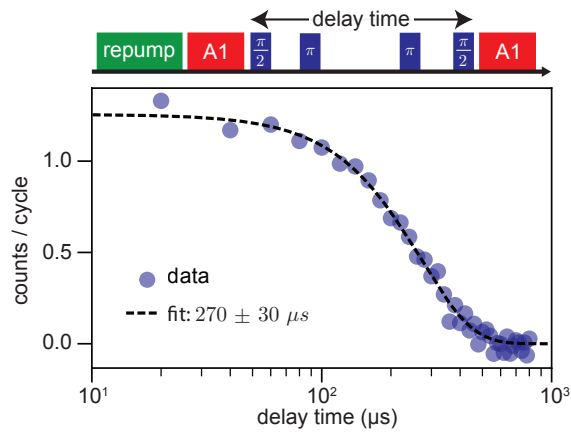


FIG. 14. Spin coherence time measured with a CPMG-2 sequence [64], measured at $|\vec{B}| = 125$ mT oriented at $\zeta = 147^\circ$. Fitting to $e^{-(t/\tau)^\xi}$ yields $\tau = 270 \pm 30 \mu\text{s}$ with stretch factor $\xi = 1.93 \pm 0.01$.

- laita, A. Safavi-Naeini, Z.-X. Shen, N. A. Melosh, S. Chu, M. Lončar, and J. Vučković, *Phys. Rev. Lett.* **121**, 083601 (2018).
- [15] C. T. Nguyen, D. D. Sukachev, M. K. Bhaskar, B. Machielse, D. S. Levonian, E. N. Knall, P. Stroganov, R. Riedinger, H. Park, M. Lončar, and M. D. Lukin, *Phys. Rev. Lett.* **123**, 183602 (2019).
- [16] M. K. Bhaskar, R. Riedinger, B. Machielse, D. S. Levonian, C. T. Nguyen, E. N. Knall, H. Park, D. Englund, M. Lončar, D. D. Sukachev, and M. D. Lukin, *Nature* **580**, 60–64 (2020).
- [17] P.-J. Stas, Y. Q. Huan, B. Machielse, E. N. Knall, A. Suleymanzade, M. Pingault, B. amd Sutula, S. W. Ding, C. M. Knaut, D. R. Assumpcao, Y.-C. Wei, M. K. Bhaskar, R. Riedinger, D. D. Sukachev, H. Park, M. Lončar, D. S. Levonian, and M. D. Lukin, *Science* **378**, 557 (2022).
- [18] C. M. Knaut, A. Suleymanzade, Y.-C. Wei, D. R. Assumpcao, P.-J. Stas, Y. Q. Huan, B. Machielse, E. N. Knall, M. Sutula, G. Baranes, N. Sinclair, C. De-Eknamkul, D. S. Levonian, M. K. Bhaskar, H. Park, M. Lončar, and M. D. Lukin, *arXiv:2310.01316* (2023).
- [19] S. Ditalia Tchernij, T. Herzig, J. Forneris, J. Küpper, S. Pezzagna, P. Traina, E. Moreva, I. P. Degiovanni, G. Brida, N. Skukan, M. Genovese, M. Jakšić, J. Meijer, and P. Olivero, *ACS Photonics* **4**, 2580 (2017).
- [20] T. Iwasaki, Y. Miyamoto, T. Taniguchi, P. Siyushev, M. H. Metsch, F. Jelezko, and M. Hatano, *Phys. Rev. Lett.* **119**, 253601 (2017).
- [21] A. E. Rugar, C. Dory, S. Sun, and J. Vučković, *Phys. Rev. B* **99**, 205417 (2019).
- [22] M. E. Trusheim, B. Pingault, N. H. Wan, M. Gündoğan, L. De Santis, R. Debroux, D. Gangloff, C. Purser, K. C. Chen, M. Walsh, J. J. Rose, J. N. Becker, B. Lienhard, E. Bersin, I. Paradeisanos, G. Wang, D. Lyzwa, A. R.-P. Montblanch, G. Malladi, H. Bakhru, A. C. Ferrari, I. A. Walmsley, M. Atatüre, and D. Englund, *Phys. Rev. Lett.* **124**, 023602 (2020).
- [23] J. Görlitz, D. Herrmann, G. Thiering, P. Fuchs, M. Gandil, T. Iwasaki, T. Taniguchi, M. Kieschnick, J. Meijer, M. Hatano, A. Gali, and C. Becher, *New J. Phys.* **22**, 013048 (2020).
- [24] I. Karapatzakis, J. Resch, M. Schrodin, P. Fuchs, M. Kieschnick, J. Heupel, L. Kussi, C. Surgers, C. Popov, J. Meijer, C. Becher, W. Wernsdorfer, and D. Hunger, <https://arxiv.org/abs/2403.00521> (2024).
- [25] R. Debroux, C. P. Michaels, C. M. Purser, N. Wan, M. E. Trusheim, J. Arjona Martínez, R. A. Parker, A. M. Stramma, K. C. Chen, L. de Santis, E. M. Alexeev, A. C. Ferrari, D. Englund, D. A. Gangloff, and M. Atatüre, *Phys. Rev. X* **11**, 041041 (2021).
- [26] E. I. Rosenthal, C. P. Anderson, H. C. Kleidermacher, A. J. Stein, H. Lee, J. Grzesik, G. Scuri, A. E. Rugar, D. Riedel, S. Aghaeimebodi, G. H. Ahn, K. Van Gasse, and J. Vučković, *Phys. Rev. X* **13**, 031022 (2023).
- [27] X. Guo, A. M. Stramma, Z. Li, W. G. Roth, B. Huang, Y. Jin, R. A. Parker, J. Arjona Martínez, N. Shofer, C. P. Michaels, C. P. Purser, M. H. Appel, E. M. Alexeev, T. Liu, A. C. Ferrari, D. D. Awschalom, N. Deegan, B. Pingault, G. Galli, F. J. Heremans, M. Atatüre, and A. A. High, *Phys. Rev. X* **13**, 041037 (2023).
- [28] A. E. Rugar, C. Dory, S. Aghaeimebodi, H. Lu, S. Sun, S. Deb Mishra, Z.-X. Shen, N. A. Melosh, and J. Vučković, *ACS Photonics* **7**, 2356–2361 (2020).
- [29] A. E. Rugar, S. Aghaeimebodi, D. Riedel, C. Dory, H. Lu, P. J. McQuade, Z.-X. Shen, N. A. Melosh, and J. Vučković, *Phys. Rev. X* **11**, 031021 (2021).
- [30] K. Kuruma, B. Pingault, C. Chia, D. Renaud, P. Hoffmann, S. Iwamoto, C. Ronning, and M. Lončar, *Applied Physics Letters* **118**, 230601 (2021).
- [31] J. Arjona Martínez, R. A. Parker, K. C. Chen, C. M. Purser, L. Li, C. P. Michaels, A. M. Stramma, R. Debroux, I. B. Harris, M. Hayhurst Appel, E. C. Nichols, M. E. Trusheim, D. A. Gangloff, D. Englund, and M. Atatüre, *Phys. Rev. Lett.* **129**, 173603 (2022).
- [32] R. A. Parker, J. Arjona Martínez, K. C. Chen, A. M. Stramma, I. B. Harris, C. P. Michaels, M. E. Trusheim, M. H. Appel, C. M. Purser, W. G. Roth, D. Englund, and M. Atatüre, *Nature Photonics* **18**, 156–161 (2024).
- [33] M. Pasini, N. Codreanu, T. Turan, A. Riera Moral, C. F. Primavera, L. De Santis, H. K. C. Beukers, J. M. Brevoord, C. Waas, J. Borregaard, and R. Hanson, *arXiv:2311.12927* (2023).
- [34] Y. Herrmann, J. Fischer, J. M. Brevoord, C. Sauerzapf, L. G. C. Wienhoven, L. J. Feije, M. Pasini, M. Eschen, M. Ruf, M. J. Weaver, and R. Hanson, *arXiv:2311.08456* (2023).
- [35] J. M. Brevoord, L. De Santis, T. Yamamoto, M. Pasini, N. Codreanu, T. Turan, H. K. C. Beukers, C. Waas, and R. Hanson, *arXiv:2311.11962* (2023).
- [36] I. B. Harris, C. P. Michaels, K. C. Chen, R. A. Parker, M. Titze, J. Arjona Martínez, M. Sutula, I. R. Christen, A. M. Stramma, W. Roth, C. M. Purser, M. H. Appel, C. Li, M. E. Trusheim, N. L. Palmer, M. L. Markham, E. S. Bielejec, M. Atatüre, and D. Englund, *PRX Quantum* **4**, 040301 (2023).
- [37] L. Orphal-Kobin, C. G. Torun, J. M. Bopp, G. Pieplow, and T. Schröder, *arXiv:2312.06431* (2023).
- [38] G. Pieplow, M. Belhassen, and T. Schröder, *Phys. Rev. B* **109**, 115409 (2024).
- [39] J. Görlitz, D. Herrmann, P. Fuchs, T. Iwasaki, T. Taniguchi, D. Rogalla, D. Hardeman, P.-O. Colard, M. Markham, M. Kieschnick, J. Meijer, M. Hatano, and C. Becher, *npj Quantum Information* **8**, 45 (2022).

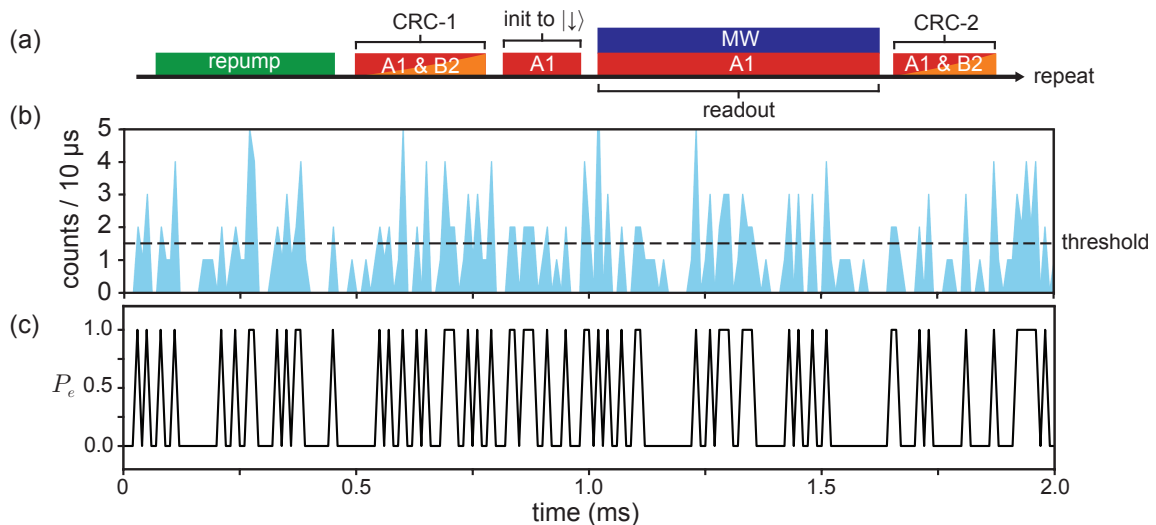


FIG. 15. Discrete quantum jumps of the electron spin measured continuously. (a) The measurement sequence consists of a green repump, followed by spin-initialization and continuous readout of the same state in the presence of a weak microwave drive (≈ 1 dBm at the sample). CRCs are implemented before and after the readout step. (b) Time trace of the collected fluorescence (in $10 \mu\text{s}$ bins showing discrete “high” ($N_r \geq 2$) counts which are real-time jumps of the electron. (c) The same time trace of the quantum jumps with assigned spin state as “0” or “1” based on the discrimination threshold (N_r).

- [40] G. Thiering and A. Gali, *Phys. Rev. X* **8**, 021063 (2018).
- [41] C. Foot, *Atomic Physics* (Oxford, 2005).
- [42] L. Robledo, L. Childress, H. Bernien, B. Hensen, P. F. A. Alkemade, and R. Hanson, *Nature* **477**, 574–578 (2011).
- [43] J. M. Kindem, A. Ruskuc, J. G. Bartholomew, J. Rochman, Y. Q. Huan, and A. Faraon, *Nature* **580**, 201–204 (2020).
- [44] X.-Y. Lai, R.-Z. Fang, T. Li, R.-Z. Su, J. Huang, H. Li, L.-X. You, X.-H. Bao, and J.-W. Pan, arXiv:2401.04470 (2024).
- [45] A. Lupașcu, S. Saito, T. Picot, P. C. De Groot, C. J. P. M. Harmans, and J. E. Mooij, *Nature Physics* **3**, 119–123 (2007).
- [46] M. Raha, S. Chen, C. M. Phenicie, S. Ourari, A. M. Dibos, and J. D. Thompson, *Nature Communications* **11**, 1605 (2020).
- [47] J. Preskill, *California Institute of Technology* **16**, 1 (1998).
- [48] D. Riedel, H. Lee, J. F. Herrmann, J. Grzesik, V. Ansari, J.-M. Borit, H. S. Stokowski, S. Aghaeimeibodi, H. Lu, P. J. McQuade, N. A. Melosh, Z.-X. Shen, A. H. Safavi-Naeini, and J. Vučković, *ACS Photonics* **10**, 4236 (2023).
- [49] C. Dory, D. Vercruyssen, K. Y. Yang, N. V. Sapral, A. E. Rugar, S. Sun, D. M. Lukin, A. Y. Piggott, J. L. Zhang, M. Radulaski, K. G. Lagoudakis, L. Su, and J. Vučković, *Nature Communications* **19**, 3309 (2019).
- [50] M. J. Burek, C. Meuwly, R. E. Evans, M. K. Bhaskar, A. Sipahigil, S. Meesala, B. Machielse, D. D. Sukachev, C. T. Nguyen, J. L. Pacheco, E. Bielejec, M. D. Lukin, and M. Lončar, *Phys. Rev. Appl.* **8**, 024026 (2017).
- [51] A. A. Clerk, M. H. Devoret, S. M. Girvin, F. Marquardt, and R. J. Schoelkopf, *Rev. Mod. Phys.* **82**, 1155 (2010).
- [52] C. C. Bultink, B. Tarasinski, N. Haandbæk, S. Poletto, N. Haider, D. J. Michalak, A. Bruno, and L. DiCarlo, *Applied Physics Letters* **112**, 092601 (2018).
- [53] E. I. Rosenthal, C. M. F. Schneider, M. Malnou, Z. Zhao, F. Leditzky, B. J. Chapman, W. Wustmann, X. Ma, D. A. Palken, M. F. Zanner, L. R. Vale, G. C. Hilton, J. Gao, G. Smith, G. Kirchmair, and K. W. Lehnert, *Phys. Rev. Lett.* **126**, 090503 (2021).
- [54] F. Lecocq, L. Ranzani, G. A. Peterson, K. Cicak, X. Y. Jin, R. W. Simmonds, J. D. Teufel, and J. Aumentado, *Phys. Rev. Lett.* **126**, 020502 (2021).
- [55] T. White, A. Opremcak, G. Sterling, A. Korotkov, D. Sank, R. Acharya, M. Ansmann, F. Arute, K. Arya, J. C. Bardin, A. Bengtsson, A. Bourassa, J. Bo-vaird, L. Brill, B. B. Buckley, D. A. Buell, T. Burger, B. Burkett, N. Bushnell, Z. Chen, B. Chiaro, J. Co-gan, R. Collins, A. L. Crook, B. Curtin, S. Demura, A. Dunsworth, C. Erickson, R. Fatemi, L. F. Burgos, E. Forati, B. Foxen, W. Giang, M. Giustina, A. G. Dau, M. C. Hamilton, S. D. Harrington, J. Hilton, M. Hoffmann, S. Hong, T. Huang, A. Huff, J. Iveland, E. Jeffrey, M. Kieferová, S. Kim, P. V. Klimov, F. Kostritsa, J. M. Kreikebaum, D. Landhuis, P. Laptev, L. Laws, K. Lee, B. J. Lester, A. Lill, W. Liu, A. Locharla, E. Lucero, T. McCourt, M. McEwen, X. Mi, K. C. Miao, S. Montazeri, A. Morvan, M. Neeley, C. Neill, A. Nersisyan, J. H. Ng, A. Nguyen, M. Nguyen, R. Potter, C. Quintana, P. Roushan, K. Sankaragomathi, K. J. Satzinger, C. Schuster, M. J. Shearn, A. Shorter, V. Shvarts, J. Skrzynny, W. C. Smith, M. Szalay, A. Torres, B. W. K. Woo, Z. J. Yao, P. Yeh, J. Yoo, G. Young, N. Zhu, N. Zobrist, Y. Chen, A. Megrant, J. Kelly, and O. Naaman, *Appl. Phys. Lett.* **122**, 014001 (2023).
- [56] M. S. Blok, C. Bonato, M. L. Markham, D. J. Twitchen, V. V. Dobrovitski, and R. Hanson, *Nature Physics* **10**, 189–193 (2014).
- [57] G.-Q. Liu, J. Xing, W.-L. Ma, P. Wang, C.-H. Li, H. C. Po, Y.-R. Zhang, H. Fan, R.-B. Liu, and X.-Y. Pan, *Phys. Rev. Lett.* **118**, 150504 (2017).

- [58] M. Pfender, P. Wang, H. Sumiya, S. Onoda, W. Yang, D. Bhaktavatsala, R. Dasari, P. Neumann, X.-Y. Pan, J. Isoya, R.-B. Liu, and J. Wrachtrup, *Nature Communications* **10**, 594 (2019).
- [59] K. S. Cujia, J. M. Boss, K. Herb, J. Zopes, and C. L. Degen, *Nature* **571**, 230–233 (2019).
- [60] J. Feder, A. Bourassa, mtsolmn, bensoloway, jamendez99, mendezUC, and A. Jones, Zenodo , nspyre (2023).
- [61] J. R. Johansson, P. D. Nation, and F. Nori, *Comp. Phys. Comm.* **184**, 1760–1772 (2012).
- [62] B. D’Anjou and W. A. Coish, *Phys. Rev. A* **89**, 012313 (2014).
- [63] C. P. Anderson, E. O. Glen, C. Zeledon, A. Bourassa, Y. Jin, Y. Zhu, C. Vorwerk, A. L. Crook, H. Abe, J. Ul-Hassan, T. Ohshima, N. T. Son, G. Galli, and D. D. Awschalom, *Science Advances* **8**, 5 (2022).
- [64] H. Y. Carr and E. M. Purcell, *Phys. Rev.* **94**, 630 (1954).